Reduced tight-binding models for elemental Si and N, and ordered binary Si-N systems

J. Gehrmann and D. G. Pettifor
Department of Materials, University of Oxford, Oxford OX1 3PH, United Kingdom

A. N. Kolmogorov
Department of Physics, Binghamton University-SUNY, New York 13902, USA

M. Reese, M. Mrovec, and C. Elsässer
Fraunhofer-Institute for Mechanics of Materials IWM, 79108 Freiburg, Germany
and IZBS, University of Karlsruhe, 76131 Karlsruhe, Germany

R. Drautz
Atomistic Modelling and Simulation, ICAMS, Ruhr-Universität Bochum, 44801 Bochum, Germany
(Received 30 August 2014; revised manuscript received 9 January 2015; published 19 February 2015)

Silicon nitride is a bulk and a coating material exhibiting excellent mechanical properties. We present a transferable reduced tight-binding (TB) model for the silicon nitride system, developed within the framework of coarse graining the electronic structure from density-functional theory (DFT) to tight binding (TB) to bond-order potentials (BOPs). The TB bond integrals are obtained directly from mixed-basis DFT projections of wave functions onto a minimal basis of atom-centered orbitals. This approach reduces the number of overall parameters to be fitted. Furthermore, applying the reduced TB approximation automatically leads to a single σ bond order that contributes to the bond energy. DFT binding energies of ground state and metastable crystal structures are used as the benchmark to which the TB repulsive parameters are fitted. The quality of the TB models is demonstrated by comparing their predictions for the binding energies, heats of formation, elastic constants, and defect energies with DFT and experimental values.

DOI: 10.1103/PhysRevB.91.054109 PACS number(s): 71.15.Nc, 71.20.Nr, 61.72.J−

I. INTRODUCTION

Silicon nitride is one of the most widely used nonoxide ceramics and is employed in the bulk and as coatings in many applications, ranging from automotive to microelectronic industries [1–3]. Due to their high strength, hardness, and wear resistance, low density and friction coefficient, and excellent chemical and thermal stability, silicon nitride ceramics are applied in many areas at both low and high temperatures [4]. Examples include gas turbines, heat exchangers, car engine parts, fans, unlubricated roller and ball bearings, valves, seals, and crucibles for molten metal [5,6].

In addition to the application of silicon nitride in the bulk, silicon nitride films play an important role in microelectronic technology [7] and microsystem technology [8]. Due to the material's chemical resistance, ease of deposition with various processes, and etching properties (especially the etching rate compared to silicon), silicon nitride is employed in a variety of semiconductor manufacturing processes [9]. Applications include sacrificial layers, masks, and passivation layers [10,11]. In microelectronic technology for instance, mainly amorphous silicon nitride is applied due to its low electrical conductivity, high dielectric constant, high resistance against radiation, high temperature stability, and its high barrier against alkali-ion migration and impurity diffusion. Furthermore, silicon nitride is applied in integrated circuits as dielectrics in capacitors and transistors. Silicon nitride coatings are also widely employed for their mechanical properties and are used against wear and corrosion both by itself and in composite coatings in combination with other materials like silicon carbide, titanium carbide, titanium nitride, and aluminum oxide [12–14]. In order to investigate deposition processes of silicon nitride on the atomistic level and understand the complex interatomic and interface processes, the availability of accurate and yet computationally efficient models is crucial.

The electronic structure of silicon nitride has been intensively studied with the tight-binding method by Robertson *et al.* in order to help elucidate the nature of the defects in amorphous silicon nitride [15–19]. Interatomic potentials have also been developed for the atomistic simulation of crystalline and amorphous silicon nitride using either the covalent bond-order-type Tersoff potential [20] or the two- and three-body Vashishta [21] potential that describes both ionic pairwise and covalent bond-bending interactions.

An empirical potential of the Tersoff form for interactions between silicon and nitrogen has been published by de Brito Mota *et al.* [22–24]. They fitted their parameters to a set of *ab initio* and experimental data which included experimental lattice parameters of the crystalline β-Si_3N_4 phase, *ab initio* values for the average binding energy of β-Si_3N_4, experimental equilibrium interatomic distance and binding energy of the N_2 molecule, and the *ab initio* result for the structure of the silicon-nitrogen bonds in the Si_3NH_9 molecule. This potential provides a description of amorphous silicon nitride in a wide range of nitrogen contents, from pure silicon to stoichiometric Si_3N_4, but includes only a repulsive nitrogen-nitrogen interaction and therefore unphysically prevents nitrogen-nitrogen bond formation. Despite the nonattractive nitrogen-nitrogen interaction, this parametrization has been applied to simulations of deposition [25,26] and deposition related [27] processes.

The Vashishta potential, which is similar to the form proposed by Stillinger and Weber [28] but explicitly includes an ionic term resulting from charge transfer in the two-body part, was first introduced for silicon oxide [21] and was later extended to silicon nitride [29,30]. Comparisons between molecular dynamics simulation results using this potential and experimental results showed that bond lengths for both crystalline and amorphous Si_3N_4 are in good agreement, the static structure factor is in agreement with neutron-scattering experiments, and elastic properties are within 10% of experimental data [31]. Although the Vashishta potential for silicon nitride has been used to study crack propagation and surfaces [29], pores and interfaces [31], amorphous silicon nitride [32], dynamic fracture [33], and shearing deformation [34], the potentials transferability to structures or environments not included in the fitting database is poor. For example, when modeling the interface between silicon and Si_3N_4 [35], the silicon atoms in silicon bulk, silicon nitride bulk, and the interface were all treated differently. This casts doubt on its ability to model realistically the growth of silicon nitride on a silicon substrate. To our knowledge, the Vashishta potential for silicon nitride was only applied once [36] to study the film growth of silicon nitride by molecular dynamics simulations. Unfortunately, only results of the mean cluster size but no results of local atomic environments, microstructural features, surface reconstructions, or bulk properties resulting from deposition were reported.

Ideally, one would like to represent the atomic interactions of the silicon nitride system with a quantum mechanical approach, treating the electronic degrees of freedom explicitly. This has been done with *ab initio* methods to investigate the structural stability of silicon nitride crystal phases [37–41]. However, due to the restriction of computing power, only simulations using empirical interatomic potentials, which often lack transferability and accuracy, can reach the length and time scales necessary to study phenomena such as film growth, nanoindentation, radiation damage, and dislocation dynamics. Nevertheless, in contrast to empirical potentials, bond-based bond-order potentials (BOPs) could provide an accurate description of a wide array of local atomic environments in covalent systems [42]. Generally, analytic BOPs can be derived either for metals [43] or semiconductors [44,45] by coarse graining the electronic structure from density functional theory (DFT) to tight binding (TB) to BOPs. Within this approach, the TB parameters can be extracted directly from DFT by projecting the wave functions onto a minimal basis of atom-centered orbitals [46,47]. In the particular case of bond-based BOPs, reduced TB links the quantum mechanical with the atomistic level. The BOPs are interatomic potentials for which the time for energy and force computations scales linearly with system size. For a given number of atoms, the BOPs are about 10–100× more computationally expensive than the empirical potentials discussed above. For very small simulations with only a handful of atoms the reduced TB calculations are approximately a factor of 10 slower than the BOPs, however, due to the cubic scaling of the time for a force or energy computation with the number of atoms the TB calculations become computationally expensive for simulations with more than a few thousand atoms. Standard DFT implementations show the same scaling as TB, but are still orders of magnitude more expensive.

Here we show that reduced TB is not just a theoretical coarse-graining step in the development process of bond-based BOPs, but, in addition, provides a transferable interatomic potential for the silicon nitride system. Furthermore, it is known that interatomic electronic charge redistribution is present in heterovalent compounds such as silicon nitride due to the large Pauling electronegativity difference between the atomic species [48]. This results in a hybrid of covalent and ionic bonding. We have included charge transfer within a self-consistent density-functional tight-binding scheme [49].

This paper is structured as follows. In Sec. II we outline the methodology behind the development of our transferable reduced TB models. In particular, in Sec. II A we describe the step from DFT to TB and in Sec. II B the step from TB to reduced TB. In Secs. III to V we present the three reduced TB models for silicon, nitrogen, and silicon nitride, respectively. Finally, we conclude in Sec. VI.

II. METHODOLOGY

A. From DFT to TB

1. Orthogonal TB bond integrals

TB approaches present a chemically intuitive approximation to the quantum mechanical electronic structure. While DFT methods explicitly calculate the Hamiltonian using a large number of basis functions, TB methods utilize parametrized forms of Hamilton and overlap matrices, typically as simple (analytical or numerical) functions of the distance between two atoms. Orthogonal tight-binding (OTB) schemes, whose overlap matrix is the unity matrix, then require just a small set of parameters describing the chemical bonding: the intersite elements

$$H_{i\alpha j\beta} = \langle i\alpha|\hat{H}|j\beta\rangle, \tag{1}$$

known as bond or hopping integrals, between valence orbitals $i\alpha$ and $j\beta$, and the on-site elements

$$H_{i\alpha i\alpha} = \langle i\alpha|\hat{H}|i\alpha\rangle, \tag{2}$$

characterizing the orbital energies. These quantities can be obtained directly from DFT calculations using the screened LMTO method [50] or various projection schemes [46,47] and do not need to be fitted in an empirical way.

Another characteristic feature of TB models is employment of only a minimal basis of atomiclike atomic orbitals. Specifically for main group elements such as Si and N, it is sufficient to consider s and p orbitals only. In this case, the elemental OTB models contain just four types of bond integrals termed $ss\sigma$, $sp\sigma$, $pp\sigma$, and $pp\pi$, and two on-site terms $E_s^{(0)}$ and $E_p^{(0)}$, according to the classical notation of Slater and Koster [51]. For the particular case of $\alpha = s$ and $\beta = s$, Eq. (1) then relates to the Slater and Koster notation as

$$H_{isjs} = \langle is|\hat{H}|js\rangle = ss\sigma_{ij}. \tag{3}$$

In the present work we obtained these quantities using the recent projection scheme of Urban *et al.* [46]. This approach is based on constructing a minimal basis of optimized atomic orbitals which give the best possible representation of the

electronic wave functions from self-consistent DFT calculations for selected atomic structures and bonding environments. The main advantage of this procedure, applied recently to the binary titanium carbide and titanium nitride systems [52], is that it provides a consistent, physically based set of parameters whose validity and range of applicability is known.

2. *Binding energy*

For the development of the reduced TB models we use DFT binding energy curves of a structure database as a benchmark. The computational details of the DFT calculations are described in Sec. II C.

The local charge neutrality (LCN) constraint is a reasonable approximation for elemental silicon and nitrogen systems. In this case, the binding energy can be expressed as [43]

$$U_B^{(\mathrm{LCN})} = U_{\mathrm{bond}} + U_{\mathrm{prom}} + U_{\mathrm{rep}} + \Delta U_{\mathrm{atom}}, \tag{4}$$

where the bond energy can be written in the on-site representation as

$$U_{\mathrm{bond}} = \sum_{i\alpha} \int_{-\infty}^{E_F} (E - E_{i\alpha}) n_{i\alpha}(E) dE. \tag{5}$$

E_F is the Fermi energy, $E_{i\alpha}$ is the on-site energy level, and $n_{i\alpha}(E)$ is the local density of states (LDOS) projected onto atom i and orbital α for both up and down spins. Alternatively, the bond energy can be written in the intersite representation as a sum over contributions from individual bonds between atomic sites i and j,

$$U_{\mathrm{bond}} = \sum_{i,j:i<j} U_{\mathrm{bond},ij}, \tag{6}$$

with

$$U_{\mathrm{bond},ij} = 2 \sum_{\alpha,\beta} H_{i\alpha j\beta} \Theta_{j\beta i\alpha}. \tag{7}$$

The matrix element of the bond-order operator $\hat{\Theta}$ with respect to the valence orbitals $|i\alpha\rangle$ and $|j\beta\rangle$ is given by

$$\Theta_{i\alpha j\beta} = \langle i\alpha | \hat{\Theta} | j\beta \rangle. \tag{8}$$

The expression in Eq. (7) is multiplied by two to account for the assumed spin degeneracy of nonmagnetic systems.

U_{prom} is the energy contribution resulting from promoting electrons between different levels compared to the free atom occupation and is therefore associated with the formation of hybrid orbitals [43],

$$U_{\mathrm{prom}} = \sum_{i\alpha} E_{i\alpha}^{(0)} q_{i\alpha}. \tag{9}$$

$E_{i\alpha}^{(0)}$ is the reference level, which we take as the free atom on-site energy level, and $q_{i\alpha}$ is the difference between the number of electrons on a tightly bound and a free atom i and orbital α [43],

$$q_{i\alpha} = N_{i\alpha} - N_{i\alpha}^{(0)}. \tag{10}$$

Therefore, LCN on each atom i is met by

$$q_i = \sum_{\alpha} q_{i\alpha} = 0. \tag{11}$$

Both the repulsive pair potential and the two-center bond integrals are represented by generalized GSP analytic functions [53,54] $f_{\mathrm{GSP}}(R)$ that are cut off smoothly from $R = R_{\mathrm{tail}}$ by the exponential-cosine cutoff function $f_{\mathrm{cut}}(R)$ that vanishes for $R = R_{\mathrm{cut}}$. Thus,

$$f(R) = f_{\mathrm{GSP}}(R) + f_{\mathrm{cut}}(R), \tag{12}$$

where

$$f_{\mathrm{GSP}}(R) = \left(\frac{R_0}{R}\right)^{n_a} \exp\left\{n_b \left[\left(\frac{R_0}{R_c}\right)^{n_c} - \left(\frac{R}{R_c}\right)^{n_c}\right]\right\} \quad \text{for } R < R_{\mathrm{tail}}, \tag{13}$$

and

$$f_{\mathrm{cut}}(R) = \frac{1}{2} f_0 \exp\{(f_0'/f_0)(R - R_{\mathrm{tail}})\} \times \left[1 - \cos\left(\pi \frac{R - R_{\mathrm{cut}}}{R_{\mathrm{cut}} - R_{\mathrm{tail}}}\right)\right] \quad \text{for } R_{\mathrm{tail}} \leqslant R \leqslant R_{\mathrm{cut}}, \tag{14}$$

with the matching boundary conditions

$$f_{\mathrm{cut}}(R_{\mathrm{tail}}) = f_{\mathrm{GSP}}(R_{\mathrm{tail}}) = f_0, \tag{15}$$

$$f_{\mathrm{cut}}'(R_{\mathrm{tail}}) = f_{\mathrm{GSP}}'(R_{\mathrm{tail}}) = f_0'. \tag{16}$$

The repulsive energy is then approximated by

$$U_{\mathrm{rep}} = \sum_i \left(\sum_{j:i<j} \phi_{ij}(R)\right)^{n_{d,i}} + \sum_{i,j:i<j} Y_{ij}(R), \tag{17}$$

with the repulsive pair potential

$$\phi(R) = \phi_0 f(R), \tag{18}$$

and a Yukawa-type core repulsion

$$Y(R) = a_c R^{-b_c} \exp(-c_c R). \tag{19}$$

The latter is needed at very short interatomic distances for the elemental silicon and the binary silicon nitride interactions to repel strongly enough to avoid fusion of silicon silicon and silicon nitrogen pairs. Note that nitrogen has no p core electrons while silicon does, and, therefore, has a softer core that allows the formation of dimeric N_2 as its ground state (see, e.g., Sec. 4.2 of Ref. [48]). The Yukawa-type term is cut off smoothly in the same fashion as described above. $n_{d,i}$ in Eq. (17) is an embedding exponent. Similar to the repulsive potential $\phi(R)$ in Eq. (18), the bond integrals are written

$$\beta(R) = \beta_0 f(R), \tag{20}$$

with $n_a = n_b$ in Eq. (13).

ΔU_{atom} in Eq. (4) accounts for the upward shift of the nonmagnetic DFT free atom reference energy compared to the magnetic free atom value due to the atom's spin configuration,

$$\Delta U_{\mathrm{atom}} = \sum_i \Delta U_{\mathrm{atom},i}. \tag{21}$$

For most elemental systems LCN is a reasonable approximation. However, for the binary silicon nitride system where the difference in electronegativity between silicon and nitrogen drives charge redistribution between the sites, the explicit

inclusion of charge transfer (CT) is crucial. (The Pauling electronegativity values for silicon and nitrogen are 1.90 and 3.04, respectively.) This leads to the following expression for the binding energy:

$$U_B^{(CT)} = U_{\text{bond}} + U_{\text{prom}} + U_{\text{ion}}^{\text{intra}} + U_{\text{ion}}^{\text{inter}} + U_{\text{rep}} + \Delta U_{\text{atom}}. \tag{22}$$

The bond, repulsive, and free atom terms take the same form as described above, but the promotion energy now takes the form (cf. Eq. (85) Ref. [43])

$$U_{\text{prom}} = \sum_{i\alpha} E_{i\alpha}^{(0)}(q_{i\alpha} - \Delta q_{i\alpha}). \tag{23}$$

$\Delta q_{i\alpha}$ is the charge taken from or put onto atom i and orbital α due to total charge transfer

$$q_i = \sum_{\alpha} \Delta q_{i\alpha} \tag{24}$$

between atoms, where $\Delta q_{i\alpha}$ is fixed by ensuring that the resulting change in atomic energy is minimized. In contrast, $q_{i\alpha}$ is the charge on atom i and orbital α following the self-consistent optimization of the energy of the system. $q_{i\alpha}$ is equivalent to the definition in Eq. (10), although, the values of $N_{i\alpha}$ may differ from those when enforcing LCN due to nonzero values of $\Delta q_{i\alpha}$. Similar to the condition for Eq. (9) in Eq. (11), for each atom when allowing CT the following condition is met:

$$\sum_{\alpha} (q_{i\alpha} - \Delta q_{i\alpha}) = 0. \tag{25}$$

This implies that the promotion energy when allowing CT is the result of promoting electrons between different levels compared to the free atom occupation after $\Delta q_{i\alpha}$ has been taken from or put onto atom i and orbital α.

$U_{\text{ion}}^{\text{intra}}$ in Eq. (22) is the energy to form ions,

$$U_{\text{ion}}^{\text{intra}} = \sum_i \left(\overline{E}_i q_i + \frac{1}{2} J_i q_i^2 \right), \tag{26}$$

where

$$\overline{E}_i = \frac{\sum_\alpha E_{i\alpha}^{(0)} \Delta q_{i\alpha}}{q_i} \tag{27}$$

and J_i is the species dependent atomic on-site Coulomb integral. The first term of Eq. (26) is directly related to the electronegativity of atoms. This term lowers the energy of the system and drives charge transfer between atoms. The second term of Eq. (26) increases the energy of the system and thereby counteracts charge transfer between atoms. Note that the second term in Eq. (23) for the promotion energy and the first term in Eq. (26) for the ion formation energy cancel when the promotion and the ion formation energies are added together.

$U_{\text{ion}}^{\text{inter}}$ is the electrostatic energy which is responsible for the anions and cations attracting each other due to their opposing charges in an ionic solid and is defined as

$$U_{\text{ion}}^{\text{inter}} = \frac{1}{2} \sum_{i,j:i\neq j} J_{ij} q_i q_j. \tag{28}$$

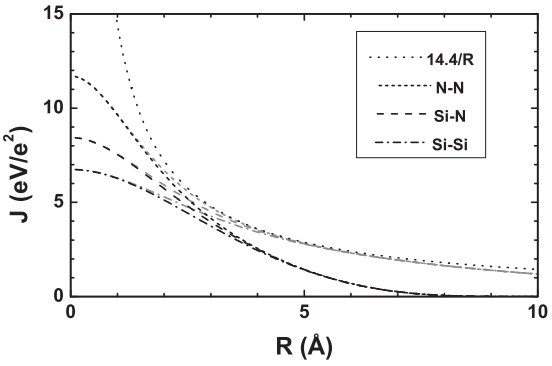

FIG. 1. Screened Coulomb integrals [56] J as a function of interatomic distance R for the elemental silicon-silicon (Si-Si) and nitrogen-nitrogen (N-N) and binary silicon-nitrogen (Si-N) interactions (black: range of function from 0 to 10 Å, gray: range of function from 0 to 30 Å) compared to the unscreened Coulomb interaction.

Figure 1 shows the Coulomb integrals of the elemental and binary interactions and the standard Coulomb interaction as a function of interatomic distance R. The functional forms for the screened Coulomb integrals of the homo- and heteronuclear interactions as a function of interatomic distance can be found in Refs. [49] and [55]. To avoid the computationally expensive Ewald summation, the Coulomb integrals are screened and truncated using a polynomial of order 7 that can be found in Ref. [56], with a range of the function defined from 0 to 10 Å. We also tested a range of the function defined from 0 to 30 Å, given in gray in Fig. 1, which resulted in the same charge transfer between the atoms.

B. From TB to reduced TB

By choosing the z axis along the direction of the bond from atom i to atom j the ij bond energy in Eq. (7) separates into individual σ and π contributions, namely

$$U_{\text{bond},ij} = U_{\text{bond},ij}^{\sigma} + U_{\text{bond},ij}^{\pi}, \tag{29}$$

with

$$U_{\text{bond},ij}^{\sigma} = 2(ss\sigma_{ij}\Theta_{jsis} + sp\sigma_{ij}\Theta_{jzis} + ps\sigma_{ij}\Theta_{jsiz} + pp\sigma_{ij}\Theta_{jziz}) \tag{30}$$

and

$$U_{\text{bond},ij}^{\pi} = 2pp\pi_{ij}(\Theta_{jxix} + \Theta_{jyiy}). \tag{31}$$

Thus, whereas the π bond energy can be written as a single contribution $2\beta_{\pi ij}\Theta_{\pi ji}^{\text{tot}}$, the σ bond energy comprises four different contributions as in Eq. (30) so that the powerful valence bond concept of a single σ bond order is lost.

For a binary sp-valent system the reduced TB approximation [57,58] reduces the *four* independent TB σ bond integrals $ss\sigma_{ij}$, $sp\sigma_{ij}$, $ps\sigma_{ij}$, and $pp\sigma_{ij}$ to *three* independent parameters, namely $\beta_{\sigma ij}$, $p_{\sigma ij}$, and $p_{\sigma ji}$ by assuming that the four TB σ bond integrals satisfy the constraint equation

$$sp\sigma_{ij}\, ps\sigma_{ij} = ss\sigma_{ij}\, pp\sigma_{ij}. \tag{32}$$

For the case of homovalent bonds the constraint equation implies that the $sp\sigma_{ij}$ bond integral is given by the physically

intuitive geometric mean of $ss\sigma_{ij}$ and $pp\sigma_{ij}$, namely

$$sp\sigma_{ij} = \sqrt{|ss\sigma_{ij}|pp\sigma_{ij}}, \tag{33}$$

noting that $ss\sigma_{ij} < 0$, $pp\sigma_{ij} > 0$, $sp\sigma_{ij} > 0$, and $ps\sigma_{ij} < 0$.

Expressions for the two reduced TB parameters $p_{\sigma ij}$ and $p_{\sigma ji}$ may be obtained by making a transformation from the atomic orbitals to *bonding* hybrids that point into the ij bond

$$|i\sigma\rangle = \sqrt{1-p_{\sigma ij}}|is\rangle + \sqrt{p_{\sigma ij}}|iz\rangle, \tag{34}$$

$$|j\sigma\rangle = \sqrt{1-p_{\sigma ji}}|js\rangle - \sqrt{p_{\sigma ji}}|jz\rangle, \tag{35}$$

and *nonbonding* hybrids that point away from the ij bond

$$|i\sigma^*\rangle = \sqrt{p_{\sigma ij}}|is\rangle - \sqrt{1-p_{\sigma ij}}|iz\rangle, \tag{36}$$

$$|j\sigma^*\rangle = \sqrt{p_{\sigma ji}}|js\rangle + \sqrt{1-p_{\sigma ji}}|jz\rangle. \tag{37}$$

The hybridization character on atom i clearly depends on its neighboring atoms j (and vice versa) and we will later show that for a binary system $p_{\sigma ij} \neq p_{\sigma ji}$ [see Eq. (46)]. We should note that the parameter p_σ, which gives the amount of p character in the bonding hybrids, has been defined to vary from 0 to 1 [42] in contrast to the original parameter $p_\sigma^{\rm orig}$ that varied from 0 to ∞ [57,58] as $p_\sigma^{\rm orig} = p_\sigma/(1-p_\sigma)$.

The values of $p_{\sigma ij}$ and $p_{\sigma ji}$ are now determined [57,58] by requiring that the ij intersite Hamiltonian with respect to the above i and j hybrids takes the diagonal form

$$H_{\sigma ij} = \begin{pmatrix} \beta_{\sigma ij} & 0 \\ 0 & 0 \end{pmatrix}, \tag{38}$$

where

$$\beta_{\sigma ij} = \langle i\sigma|H|j\sigma\rangle. \tag{39}$$

The diagonal *nonbonding* matrix element $\langle i\sigma^*|H|j\sigma^*\rangle$ with the *nonbonding* hybrids given by Eqs. (36) and (37) can then be made to vanish by choosing $p_{\sigma ij}$ and $p_{\sigma ji}$ to satisfy

$$\sqrt{p_{\sigma ij}/(1-p_{\sigma ij})} = pp\sigma_{ij}/sp\sigma_{ij} \tag{40}$$

and

$$\sqrt{p_{\sigma ji}/(1-p_{\sigma ji})} = pp\sigma_{ji}/sp\sigma_{ji} = pp\sigma_{ij}/|ps\sigma_{ij}|, \tag{41}$$

since $pp\sigma_{ji} = pp\sigma_{ij}$ and $sp\sigma_{ji} = |ps\sigma_{ij}|$. Furthermore, these values also lead to the off-diagonal matrix elements in Eq. (38) vanishing. Substituting $sp\sigma_{ij}$ and $|ps\sigma_{ij}|$ from Eqs. (40) and (41), respectively, into the constraint Eq. (32) immediately gives the relation that

$$pp\sigma_{ij} = \sqrt{p_{\sigma ij}p_{\sigma ji}/[(1-p_{\sigma ij})(1-p_{\sigma ji})]}|ss\sigma_{ij}|. \tag{42}$$

The reduced TB parameter $\beta_{\sigma ij}$ may now be found by substituting Eqs. (34) and (35) in Eq. (39) and using Eqs. (40) and (41) and is given by

$$\beta_{\sigma ij} = [1/\sqrt{(1-p_{\sigma ij})(1-p_{\sigma ji})}]ss\sigma_{ij}. \tag{43}$$

Finally, using Eqs. (40)–(43), the original four independent TB bond integrals can be expressed in terms of the three reduced TB parameters as

$$\left.\begin{matrix} ss\sigma_{ij} \\ sp\sigma_{ij} \\ ps\sigma_{ij} \\ pp\sigma_{ij} \end{matrix}\right\} = \left\{\begin{matrix} \sqrt{(1-p_{\sigma ij})(1-p_{\sigma ji})} \\ -\sqrt{(1-p_{\sigma ij})p_{\sigma ji}} \\ \sqrt{p_{\sigma ij}(1-p_{\sigma ji})} \\ -\sqrt{p_{\sigma ij}p_{\sigma ji}} \end{matrix}\right\}\beta_{\sigma ij}. \tag{44}$$

Interestingly, we see that squaring both sides and adding leads to the very simple expression for $\beta_{\sigma ij}$, namely

$$\beta_{\sigma ij} = -\sqrt{(ss\sigma_{ij})^2 + (sp\sigma_{ij})^2 + (ps\sigma_{ij})^2 + (pp\sigma_{ij})^2}, \tag{45}$$

which, unlike Eq. (43), weights all four TB bond integrals equally. In addition, this definition of $\beta_{\sigma ij}$ automatically guarantees that the second moment of the density of states is preserved in going from TB to reduced TB, even though the constraint Eq. (32) might not be accurately satisfied.

In this paper, therefore, all *three* reduced TB parameters will be defined in terms of the *four* TB bond integrals as for $\beta_{\sigma ij}$ in Eq. (45) above. It follows from Eqs. (40) and (41) and the constraint Eq. (32) that

$$p_{\sigma ij} = \tfrac{1}{2}\{1/[1+(sp\sigma_{ij}/pp\sigma_{ij})^2] + 1/[1+(ss\sigma_{ij}/ps\sigma_{ij})^2]\}, \tag{46}$$

and similarly for $p_{\sigma ji}$.

For elemental interactions, where $sp\sigma_{ij} = sp\sigma_{ji}$ and $ps\sigma_{ij} = ps\sigma_{ji}$, $p_{\sigma ij}$ and $p_{\sigma ji}$ are identical. However, for binary interactions, where $sp\sigma_{ij} \neq sp\sigma_{ji}$ and $ps\sigma_{ij} \neq ps\sigma_{ji}$, $p_{\sigma ij}$ and $p_{\sigma ji}$ give different results. Therefore, considering a binary sp-valent system that comprises two chemical species, e.g., Si and N which will be indexed by μ and ν, respectively, and taking account of Eq. (45), we can determine in total the following reduced TB parameters that contribute to the σ bonds in the system: $\beta_{\sigma ij}^{\rm SiSi}$, $\beta_{\sigma ij}^{\rm SiN}$, $\beta_{\sigma ij}^{\rm NN}$, $p_{\sigma ij}^{\rm SiSi}$, $p_{\sigma ij}^{\rm SiN}$, $p_{\sigma ij}^{\rm NSi}$, and $p_{\sigma ij}^{\rm NN}$.

Although $p_{\sigma ij}$ depends on both the nature of the μ and ν species of atoms i and j through Eq. (46), the dominance of the μ atom i over the ν atom j can be demonstrated [58] by making the geometric mean approximation that

$$\langle i\mu\alpha|H_\sigma|j\nu\beta\rangle \approx \sqrt{\langle i\mu\alpha|H_\sigma|j\mu\alpha\rangle\langle i\nu\beta|H_\sigma|j\nu\beta\rangle}. \tag{47}$$

This results in

$$\left(\frac{sp\sigma_{ij}^{\mu\nu}}{pp\sigma_{ij}^{\mu\nu}}\right)^2 \approx \frac{|ss\sigma_{ij}^{\mu\mu}|pp\sigma_{ij}^{\nu\nu}}{pp\sigma_{ij}^{\mu\mu}pp\sigma_{ij}^{\nu\nu}} = \frac{|ss\sigma_{ij}^{\mu\mu}|}{pp\sigma_{ij}^{\mu\mu}} \tag{48}$$

and

$$\left(\frac{ss\sigma_{ij}^{\mu\nu}}{ps\sigma_{ij}^{\mu\nu}}\right)^2 \approx \frac{|ss\sigma_{ij}^{\mu\mu}||ss\sigma_{ij}^{\nu\nu}|}{pp\sigma_{ij}^{\mu\mu}|ss\sigma_{ij}^{\nu\nu}|} = \frac{|ss\sigma_{ij}^{\mu\mu}|}{pp\sigma_{ij}^{\mu\mu}}. \tag{49}$$

Therefore, using Eq. (33),

$$p_{\sigma ij}^{\mu\nu} \approx \frac{pp\sigma_{ij}^{\mu\mu}}{|ss\sigma_{ij}^{\mu\mu}| + pp\sigma_{ij}^{\mu\mu}} = p_{\sigma ij}^{\mu\mu}. \tag{50}$$

Similarly,

$$p_{\sigma ij}^{\nu\mu} \approx \frac{pp\sigma_{ij}^{\nu\nu}}{|ss\sigma_{ij}^{\nu\nu}| + pp\sigma_{ij}^{\nu\nu}} = p_{\sigma ij}^{\nu\nu}. \tag{51}$$

We will see later (compare Figs. 3, 8, and 13) that this is an approximation that is confirmed by our data. Put differently, for example, the hybridization character on each silicon atom is very similar in the elemental diamond and the binary β ground state structures.

A different simplification to Eq. (46) would be if all the TB bond integrals displayed the same distance dependence, so that the *ratio* of any two bond integrals became distance invariant, thereby leading to constant values of $p_{\sigma ij}$.

The distance dependence of the reduced TB parameters $\beta_{\sigma ij}$ and $\beta_{\pi ij}$ are given by GSP functions with $n_a = n_b$ that we cut off as described in Sec. II A 2. The first nearest-neighbor distance dependence of the reduced TB parameters $p_{\sigma ij}$ will be shown to be well fitted by the exponential function [59]

$$p_\sigma(R) = 1/[1 + c\exp(-\gamma R)]. \tag{52}$$

C. Computational details

The computational details that we will use in the next three sections to derive reduced TB parameters for elemental silicon and nitrogen and binary silicon nitride systems are as follows.

The DFT reference binding energies are calculated with the VASP code [60,61] using the local density approximation (LDA) [62,63] to the exchange-correlation energy functional and the projector augmented-wave method (PAW) [64,65]. For each calculation, a sufficiently large plane-wave cutoff energy and a dense Monkhorst-Pack [66,67] type k-point mesh ensure numerical convergence for formation energy differences to within 5 meV/atom. We carry out the TB calculations using the bond-order potential from Oxford (BOPfox [68]) package, which solves the tight-binding secular equation in k space and calculates the local DOS using the tetrahedron k-space technique with Blöchl corrections [69].

The TB parameters are obtained as follows. For both, bond integral and repulsive functions, we choose the values for the parameters R_0, R_c, R_{tail}, and R_{cut} as follows. R_0 is set to the respective ground state equilibrium nearest neighbor distance (silicon diamond, nitrogen dimer, and silicon nitride β). R_c is set equidistantly between respective equilibrium first and second nearest neighbor distances. For nitrogen, R_c is set to half the value of the first and second nearest neighbor distances in the diamond structure. R_{tail} is set to where bond integral data are available for equilibrium structures, and R_{cut}, which defines the range of the model, is set to where the projected bond integral data are small. $\Delta U_{\text{atom},i}$ in Eq. (21) is chosen to be the magnitude of the free atom magnetic energy calculated with DFT. The parameters related to the bond integrals, β_0, n_a, and n_c in Eqs. (13) and (20), are fitted to DFT projected orthogonal TB bond integrals of equilibrium structures. The parameters related to the repulsive function in Eqs. (13) and (18), Φ_0, n_a, n_b, and n_c, are pairwise fitting parameters, and $n_{d,i}$ in Eq. (17) is an atomic fitting parameter. These repulsive parameters are varied to reproduce the DFT reference binding energies. Φ_0, n_a for bond integrals, n_b, and n_c are let to vary freely but are constrained to be positive to give smoothly decaying GSP functions. β_0 is treated similarly, but constrained to be negative. n_a of the repulsive function and n_d are used to affect stabilization over different nearest neighbor distances and coordination numbers, respectively. The fitting parameters related to the repulsive function Φ_0, n_b, and n_c are varied by minimizing the least squares error between DFT and TB binding energies employing a downhill simplex method.

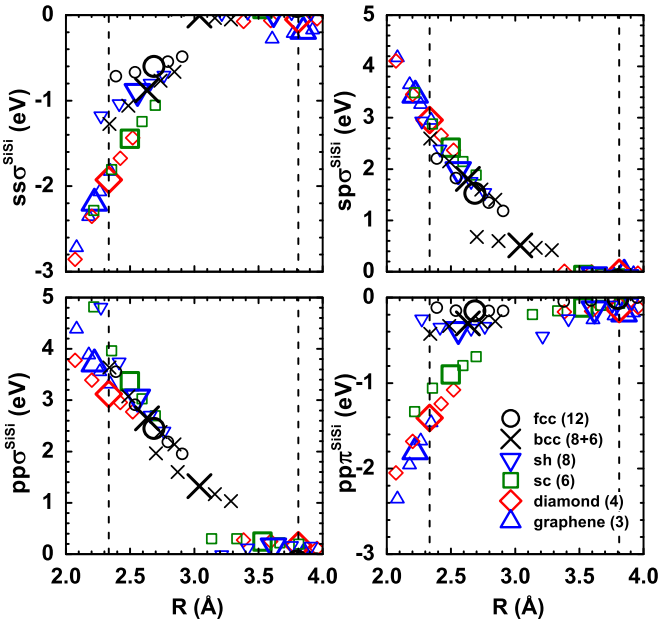

FIG. 2. (Color online) Two-center orthogonal TB Si-Si bond integrals obtained from DFT via projection scheme for different structures as a function of interatomic distance R. Equilibrium data are displayed with enlarged symbols. Dashed vertical lines are the first and second nearest neighbor distances in the ground state equilibrium diamond structure, $R_1^\diamond$ and $R_2^\diamond$.

III. REDUCED TB MODEL FOR SILICON

A. Bond integrals

The two-center orthogonal TB bond integrals obtained from DFT via the projection scheme described in Sec. II A 1 for different structures of silicon are shown in Fig. 2. In this figure and in the following, the data for equilibrium structures are displayed with enlarged symbols. As one can see from the figure, the data are distance and structure dependent. In addition, screening of the bond integrals in the second nearest neighbors data can be observed. This screening is especially visible for the bcc structure, and can be attributed to the fact that the bonding between a pair of second nearest neighbor atoms is weakened by the first nearest neighbor atoms surrounding the bond [70].

Figure 3 shows the reduced TB Si-Si parameters β_σ, β_π, and p_σ that are calculated from the data in Fig. 2 through Eqs. (45) and (46). Similar to the data in Fig. 2, the data for the reduced TB parameters β_σ, β_π, and p_σ are distance and structure dependent. The data for β_π falls off to zero at shorter values for R than the data for β_σ. This can be attributed to the relatively short range of π bonds compared to σ bonds.

The functions $\beta_\sigma(R)$, $\beta_\pi(R)$, and $p_\sigma(R)$ in Fig. 3 are fitted to equilibrium data points and cut off smoothly as described in Sec. II C. The cutoff is typically between first and second nearest neighbors of the ground state structure. In cases of steep slopes such as $\beta_\pi(R_{\text{tail}})$ in Fig. 3 a polynomial cutoff

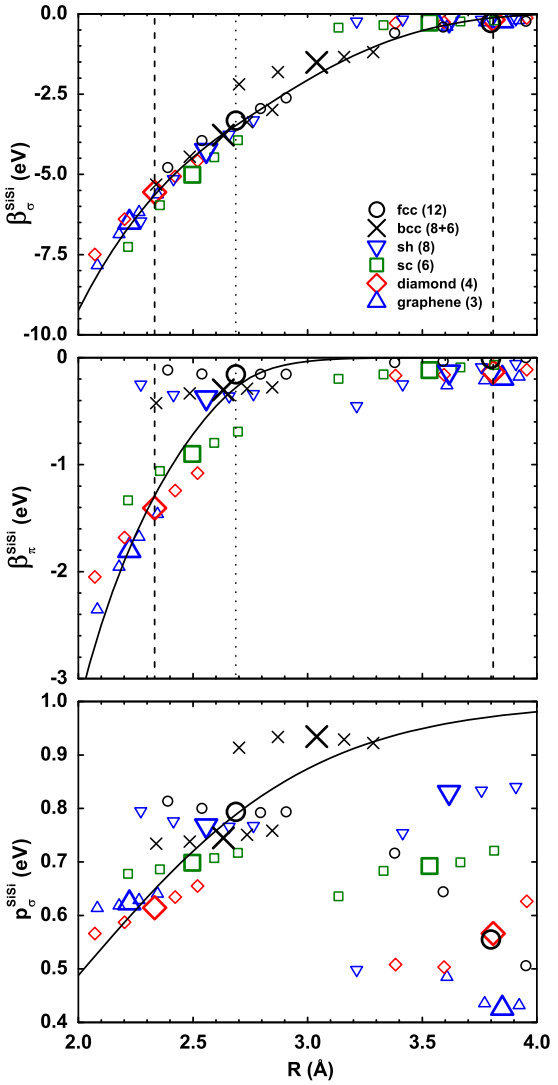

FIG. 3. (Color online) Reduced TB Si-Si parameters calculated from projected bond integrals in Fig. 2 for different structures as a function of interatomic distance R. Equilibrium data are displayed with enlarged symbols. Dashed vertical lines are the first and second nearest neighbor distances in the ground state equilibrium diamond structure, $R_1^\diamond$ and $R_2^\diamond$. The vertical dotted line marks R_{tail}.

function of degree three may lead to sign changes, and hence to a nonsmooth decay of the reduced TB parameters. However, a smooth distance dependence of the reduced TB parameters is essential for calculations of forces of nonequilibrium structures, for example in molecular dynamics simulations. The cutoff function we chose is given in Eq. (14). This function substitutes the original function over a range where the original function is not fitted, and, in contrast to a polynomial as in Xu's carbon model [71] and Kwon's silicon model [72], never changes sign.

Generally, we aim to approximate each data set with a single function. In Fig. 3 the data for β_σ are relatively structure independent unlike the individual $ss\sigma$ and $pp\sigma$ curves in Fig. 2 and the data are well reproduced by a single function. In addition, the function $\beta_\sigma(R)$ reproduces the distant-dependent gradients of all structures well. One exception is the screened

TABLE I. Reduced TB parameters for silicon-silicon (Si-Si), nitrogen-nitrogen (N-N), and silicon-nitrogen (Si-N) interactions.

	Si-Si	N-N	Si-N (N-Si)
$\beta_{0,\sigma}$ (eV)	−5.643	−21.640	−10.183
$\beta_{0,\pi}$ (eV)	−1.290	−5.015	−2.347
R_0 (Å)	2.333	1.103	1.671
R_c (Å)	3.071	2.335	2.212
$n_{a,\sigma}$	1.840	1.551	0.792
$n_{a,\pi}$	4.915	2.339	1.712
$n_{c,\sigma}$	1.080	2.937	5.005
$n_{c,\pi}$	11.552	5.382	9.009
R_{tail} (Å)	2.687	2.170	2.205
R_{cut} (Å)	4.200	2.750	3.500
c	0.333	0.976	0.588 (1.315)
γ (1/Å)	0.000	0.000	0.000 (0.000)

data of the second nearest neighbors of the bcc structure, which are equivalent to the screening effect inherent in the projected data in Fig. 2. Even though the data for β_π are more structure dependent, the gradients of the individual structures are still fairly well reproduced by a single function. The most pronounced structure dependence can be seen in the p_σ data where the nonequilibrium data and the gradients of the different structures are less well reproduced by a single function. Hence, a fit to the p_σ equilibrium data, as shown in Fig. 3, might not be the best solution as we will find in Sec. III B. The gradients of the individual structures are given in the first author's Ph.D. thesis [59].

The parameters of the functions representing the reduced TB parameters for the silicon TB model are given in Table I. In addition to the bond integrals, on-site levels are required for the reduced TB model. In this study we employ the on-site levels from Harrison [73] which are given in Table II.

Figure 4 shows the density of states of silicon diamond for DFT, projected TB, and reduced TB. For plotting reasons, all density of states are shifted along the energy scale such that the Fermi energy is at 0 eV. The features of the DFT density of states are qualitatively well reproduced by projected TB and reduced TB. Furthermore, the individual s and p contributions of the projected TB and reduced TB models reproduce the distinct sp hybridization. Whereas our current theory guarantees that the total bandwidth is conserved when going from projected TB to reduced TB, the conservation of the valence band width depends on how well reduced TB approximates the individual bond integrals for each system (see Ref. [59]).

Figure 5 displays the silicon σ and π bond orders for a first nearest neighbor bond with respect to interatomic distance in the graphene, diamond, simple cubic (sc), and face centered cubic (fcc) structures, which have coordination numbers of 3,

TABLE II. On-site levels for silicon (Si) and nitrogen (N) [73].

	Si	N
E_p (eV)	−7.59	−13.84
E_s (eV)	−14.79	−26.22

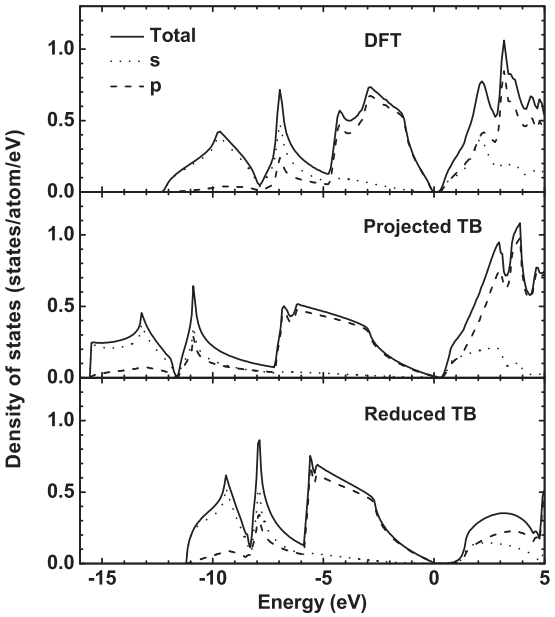

FIG. 4. *s* and *p* contributions to the average total density of states of the silicon diamond structure for DFT, projected TB, and reduced TB. For the calculation of the projected TB DOS the same on-site levels were used as for the calculation of the reduced TB DOS.

4, 6, and 12, respectively. We see that the graphene structure has a saturated σ bond together with a saturated and an unsaturated π bond corresponding to whether it lies out of or in the plane. The cubic diamond structure has a saturated σ bond and two degenerate unsaturated π bonds. Furthermore, the σ bond of the simple cubic structure is less saturated than

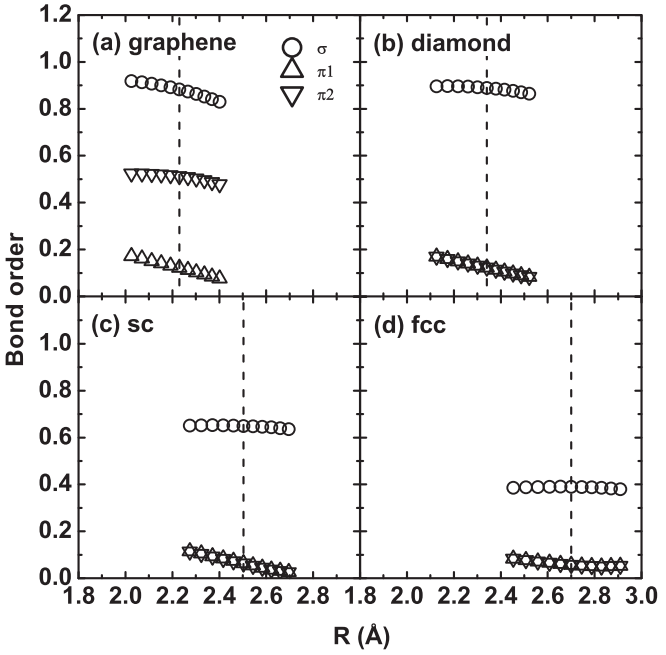

FIG. 5. σ and π bond orders for a first nearest neighbor bond in the silicon (a) graphene, (b) diamond, (c) simple cubic (sc), and (d) face centered cubic (fcc) structures as a function of interatomic distance R.

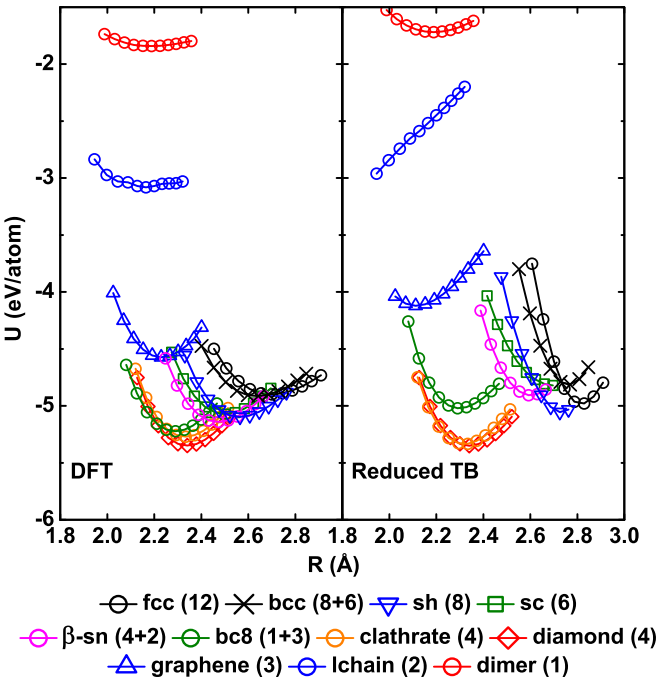

FIG. 6. (Color online) DFT and reduced TB (LCN) binding energy curves for different silicon structures as a function of nearest neighbor interatomic distance R. The number of nearest neighbors is given in parentheses for each structure.

the σ bond of the diamond structure, and the σ bond of the face centered cubic structure is the least saturated σ bond. Similar to the two π bonds of the diamond structure, the two π bonds of the simple cubic and the face centered cubic structures are perfectly degenerate. In summary, the total bond order varies inversely with the coordination number. This is in agreement with the chemistry of the investigated structure types [74].

B. Binding energy curves

Having the information for calculating the TB electronic structure, the bond and promotion energies can be computed. However, to calculate total binding energies, a repulsive function [Eq. (17)] needs to be determined. Our particular procedure is described in Sec. II C. Figure 6 displays the resulting reduced TB (LCN) binding energy curves for different silicon structures in the right-hand panel. As a comparison, the DFT binding energy curves are shown in the left-hand panel of Fig. 6. The resultant parameters of the repulsive function for the silicon reduced TB model are given in Table III. The repulsive embedding exponent n_d and the Yukawa parameters are given in Tables IV and V, respectively. The shift in the nonmagnetic compared to the magnetic reference energy of the free atom ΔU_{atom} is given in Table IV.

1. DFT binding energy curves

The binding energy curves displayed in Fig. 6 are calculated with open and close packed structures spanning a wide range of coordination. A table of all silicon structures used as a binding energy benchmark together with their equilibrium binding energies is attached as Supplemental Material [75].

TABLE III. Repulsive parameters for silicon-silicon (Si-Si), nitrogen-nitrogen (N-N), and silicon-nitrogen (Si-N) interactions.

	Si-Si	N-N	Si-N
Φ_0 (eV)	5.358	18.442	7.242
R_0 (Å)	2.333	1.103	1.671
R_c (Å)	3.071	2.335	2.212
n_a	5.000	3.328	0.010
n_b	2.210	4.017	2.456
n_c	4.170	5.709	2.890
R_{tail} (Å)	2.687	2.170	1.856
R_{cut} (Å)	4.200	2.750	4.200

These benchmark structures were used for each trial reduced TB model to compare their equilibrium reduced TB binding energies with their DFT reference binding energies.

The DFT binding energy curves in Fig. 6 show the diamond structure having the lowest binding energy, as expected. The lowest metastable structure is the clathrate structure. This structure has four nearest neighbors like diamond, but the bond lengths and angles are slightly distorted compared to those in diamond. The clathrate structure for which the data are given has 34 atoms in its unit cell. In addition, we tested a clathrate structure with 46 atoms per unit cell, which is found to have a slightly higher binding energy than clathrate 34 (DFT: 0.0073 eV/atom, reduced TB: 0.021 eV/atom). The third lowest structure is the bc8 structure. This is a body centered cubic structure with eight atoms in the basis, in which each atom has four nearest neighbors which are divided into one first and three second nearest neighbors. β-Sn is the fourth lowest structure in Fig. 6. This structure can be viewed as sixfold coordinated, because of a distinct gap between the two second nearest neighbors and the four third nearest neighbors. From the DFT binding energy data the ordering diamond $\rightarrow$ clathrate $\rightarrow$ bc8 $\rightarrow$ β-Sn is observed.

2. *Reduced TB binding energy curves*

As shown in Fig. 3 the function for p_σ does not reproduce the gradients of the reduced TB data very well. This means that choosing a distance dependent function for p_σ might not be the best choice. In fact, we found that it leads to poor fits of the binding energy curves in practice (see Ref. [59]). Instead we will see that setting p_σ to the equilibrium ground state value provides good fits to the binding energy curves. Therefore, p_σ will be chosen to be a constant by setting the parameter γ in Eq. (52) to zero (see Table I). This approach also helps us to destabilize the clathrate structure compared to the diamond structure without changing the bond integrals

TABLE IV. Embedding exponent n_d and shift in the nonmagnetic DFT free atom reference energy ΔU_{atom} for silicon (Si) and nitrogen (N).

	Si	N
n_d	0.800	1.000
ΔU_{atom} (eV)	0.611	2.888

TABLE V. Yukawa parameters.

	Si-Si	Si-N
a_c (eV)	185.000	10.444
b_c	4.500	5.794
c_c (1/Å)	0.000	−0.047
$R_{\text{tail},c}$ (Å)	1.560	1.200
$R_{\text{cut},c}$ (Å)	1.916	1.550

from having a smooth decaying character. As one can see from Fig. 6, the diamond structure is predicted to be the ground state structure by the reduced TB model. Furthermore, the ordering diamond $\rightarrow$ clathrate $\rightarrow$ bc8 $\rightarrow$ β-Sn predicted by the DFT binding energy data is reproduced by the reduced TB model. The energy differences between the diamond ground state and the bc8 and β-Sn structure are significantly larger than in DFT, such that we expect much larger pressures are necessary for a structural phase transformation compared to DFT or experiment.

In addition, the low coordinated structures dimer, linear chain (lchain), and graphene are all fairly well reproduced. Due to the hard core Yukawa potential, the binding energy of the linear chain shows a global minimum well above the diamond structure at shorter interatomic distances. The close packed structures sh, bcc, and fcc are slightly too stable compared to the DFT data. This is not generally an issue with the reduced TB methodology, but rather due to the difficulty of fitting the binding energy curves with transferable TB parameters over such a wide range of coordination.

3. *Equilibrium properties of diamond ground state*

Table VI gives equilibrium properties of silicon diamond for reduced TB (LCN) and DFT. The column named reduced TB shows the results of the reduced TB (LCN) model from this study, and the column named DFT shows the results of the DFT calculations performed in this study using LDA. The reduced TB equilibrium binding energy, equilibrium volume, and bulk modulus are in good agreement with the DFT results. In addition, the elastic constants are fairly well reproduced.

TABLE VI. Equilibrium properties of silicon diamond for reduced TB (LCN) and DFT. Equilibrium binding energy (U), equilibrium volume (V), and bulk modulus (B) are obtained from Birch-Murnaghan equation of state fits to binding energies. Units are U (eV/atom), V (Å^3), B and C (GPa).

	Reduced TB	DFT	Expt.	TB[a]
U	–5.348	–5.348	–4.63[b]	–4.620[a]
V	19.760	19.742	20.026[c]	19.999[a]
B	94	94	100[c]	100[a]
C'	63	48.5	51[d,e]	50.4[a,e]
$C44$	111	76	80[d]	75[a]

[a]Reference [76].
[b]Reference [77].
[c]Reference [78].
[d]Reference [79].
[e]Calculated from other elastic constants.

TABLE VII. Point defect formation energies in silicon diamond (eV). The numbers in parentheses in the top line are the number of atoms per perfect unit cell, whereas the pair of numbers in parentheses in the DFT column from Ref. [80] are LDA and GGA values, respectively.

	Reduced TB (128)		DFT (128)		DFT [80] (64)	TB [76] (144)	
	Unrelaxed	Relaxed	Unrelaxed	Relaxed	Relaxed	Unrelaxed	Relaxed
Vacancy	7.526	5.492	3.795	3.577	(a, a)	3.915	3.708
Split-(110)	7.743	5.327	4.949	3.340	(3.31, 3.84)	a	3.215
Hexagonal	11.839	4.862	5.961	3.378	(3.31, 3.80)	4.733	3.814
Tetrahedral	6.951	4.862	3.772	3.339	(3.43, 4.07)	4.067	3.600

[a]Not available.

Experimental data and a TB model by Lenosky *et al.* [76] are also included for comparison. We have chosen the model by Lenosky *et al.* from all the different TB fits as the most comprehensive fit to silicon diamond properties. The major difference between the Lenosky *et al.* and our approach is that Lenosky *et al.* fitted to the equilibrium properties of silicon diamond, including elastic constants, phonon frequencies, Grüneisen parameters, and point defect energies, whereas we only optimized fitting the binding energy curves. The effect of the different approaches can be seen by comparing the binding energies of the reduced TB and DFT columns with the binding energies of the experimental and Lenosky *et al.* columns.

In addition to equilibrium properties, we test the silicon reduced TB model for point defects. Table VII gives point defect formation energies in silicon. The energies are calculated using a silicon box of 128 atoms from which the defected structures are generated. This means the vacancy structure contains 127 atoms and the split-(110), hexagonal, and tetrahedral structures contain 129 atoms. The unrelaxed results are obtained from the starting configuration with the atoms being fixed with respect to the internal degrees of freedom. The relaxed results are obtained from lifting this constraint and by starting from the unrelaxed positions. The reduced TB model gives relatively high energies for the unrelaxed structures due to short interatomic distances generated by the initial configuration of the interstitial atoms where the Yukawa-type core repulsion is effective. Overall, the reduced TB model overestimates the relaxed point defect formation energies relative to DFT. Furthermore, the reduced TB model predicts an unstable hexagonal defect which relaxes into a tetrahedral defect configuration. However, despite the unstable hexagonal defect predicted by reduced TB, the energetic defect ordering tetrahedral → split-(110) → vacancy as predicted by our DFT calculations is reproduced by our reduced TB model.

IV. REDUCED TB MODEL FOR NITROGEN

A. Bond integrals

Figure 7 shows the projected two-center orthogonal TB bond integrals obtained from DFT for different structures of nitrogen. Again, the data for equilibrium structures are displayed with enlarged symbols. Compared to the silicon data in Fig. 2, the data for nitrogen are less structure dependent.

The nitrogen reduced TB parameters are displayed in Fig. 8. Similar to the two-center orthogonal TB bond integrals, the reduced TB parameters for nitrogen are less structure dependent than those displayed for silicon in Fig. 3. As expected, the β_π data are short ranged compared to the β_σ data. The functions $\beta_\sigma(R)$, $\beta_\pi(R)$, and $p_\sigma(R)$ are fitted in a similar fashion to that described for silicon.

Since the β_σ and β_π data for nitrogen in Fig. 8 are less structure dependent than that for silicon, it can be better approximated by single distance dependent functions. Overall, the functions $\beta_\sigma(R)$ and $\beta_\pi(R)$ reproduce the data values and distant-dependent gradients well. Compared to the β_σ and β_π data, the nitrogen p_σ data are more structure dependent and the gradients of the individual structures are only poorly reproduced. Again, for the same reasons given for the silicon model, we set $p_\sigma(R)$ as a constant. For nitrogen, we extrapolated the $p_\sigma(R)$ function to the dimer equilibrium distance and chose that value. This approach seems to be the best choice to achieve the correct relative ordering of metastable structures.

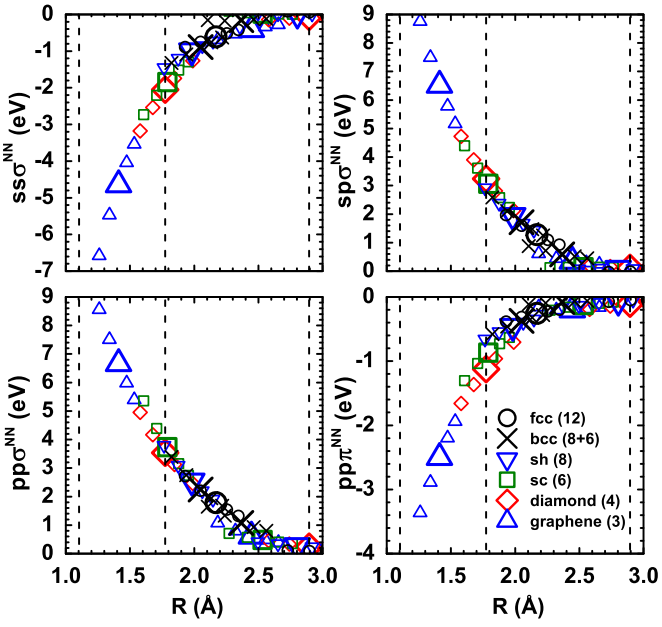

FIG. 7. (Color online) Two-center orthogonal TB N-N bond integrals obtained from DFT via projection scheme for different structures as a function of interatomic distance R. Equilibrium data are displayed with enlarged symbols. Dashed vertical lines are, from left to right, the first nearest neighbor distance in the ground state equilibrium dimer R_1^{dimer}, and the first and second nearest neighbor distances in the equilibrium diamond structure $R_1^\diamond$ and $R_2^\diamond$.

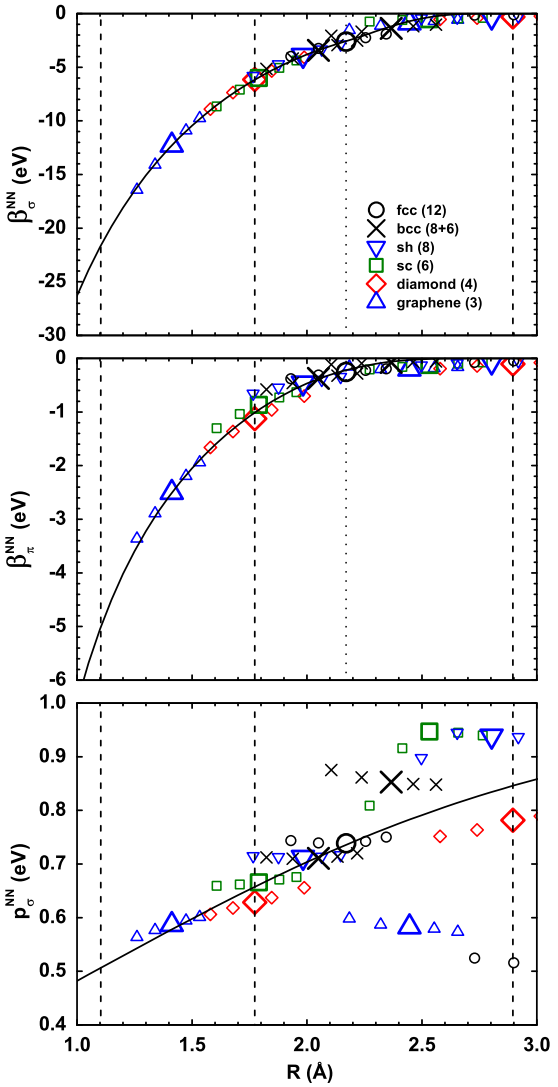

FIG. 8. (Color online) Reduced TB N-N parameters calculated from projected bond integrals in Fig. 7 for different structures as a function of interatomic distance R. Equilibrium data are displayed with enlarged symbols. Dashed vertical lines are, from left to right, the first nearest neighbor distance in the ground state equilibrium dimer R_1^{dimer}, and the first and second nearest neighbor distances in the equilibrium diamond structure $R_1^{\diamond}$ and $R_2^{\diamond}$. The vertical dotted line marks R_{tail}.

The parameters of the functions representing the reduced TB parameters for the nitrogen reduced TB model are given in Table I and the on-site levels are given in Table II.

The density of states of the nitrogen cubic gauche (cg) structure for DFT, projected TB, and reduced TB is shown in Fig. 9. The features of the DFT density of states are well reproduced by projected TB and reduced TB. Again, projected TB and reduced TB reproduce the sp-hybridization feature of the DFT density of states well.

The distance dependence of the nearest neighbor σ and π bond orders of nitrogen are displayed in Fig. 10 for the dimer, cubic gauche (cg), diamond, and simple cubic (sc) structures with coordination numbers of 1, 3, 4, and 6, respectively. The nitrogen dimer has a saturated σ bond and two saturated π bonds. The cubic gauche structure has a

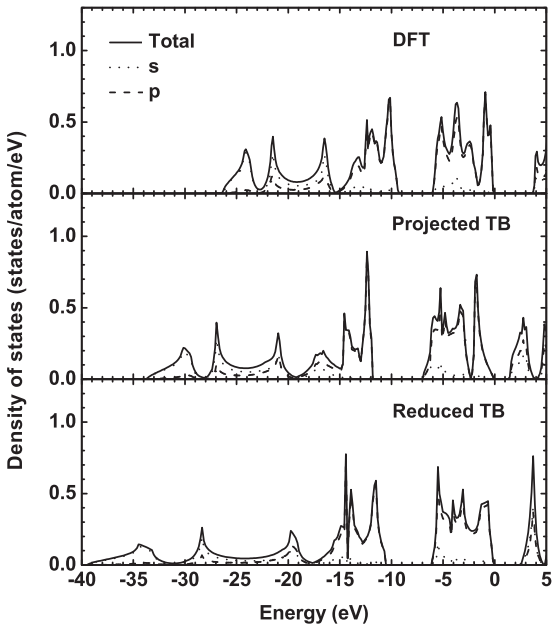

FIG. 9. s and p contributions to the average total density of states of the nitrogen cubic gauche (cg) structure for DFT, projected TB, and reduced TB. For the calculation of the projected TB DOS the same on-site levels were used as for the calculation of the reduced TB DOS.

saturated σ and two unsaturated π bonds. This is equivalent to three single bonds and a lone pair per atom. The diamond structure has one half saturated σ and two unsaturated π bonds. The character of the ij bond in the simple cubic structure is similar to the character of the ij bond in the diamond

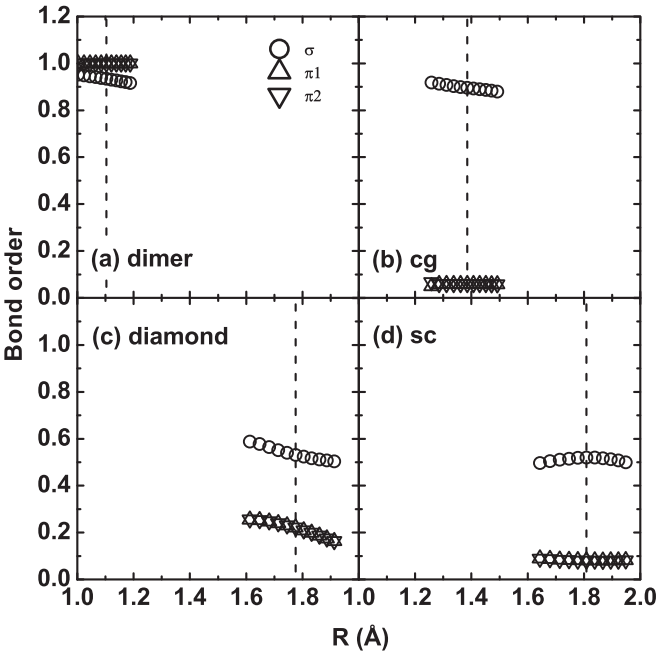

FIG. 10. σ and π bond orders for a first nearest neighbor bond in the nitrogen (a) dimer, (b) cubic gauche (cg), (c) diamond, and (d) simple cubic (sc) structures as a function of interatomic distance R.

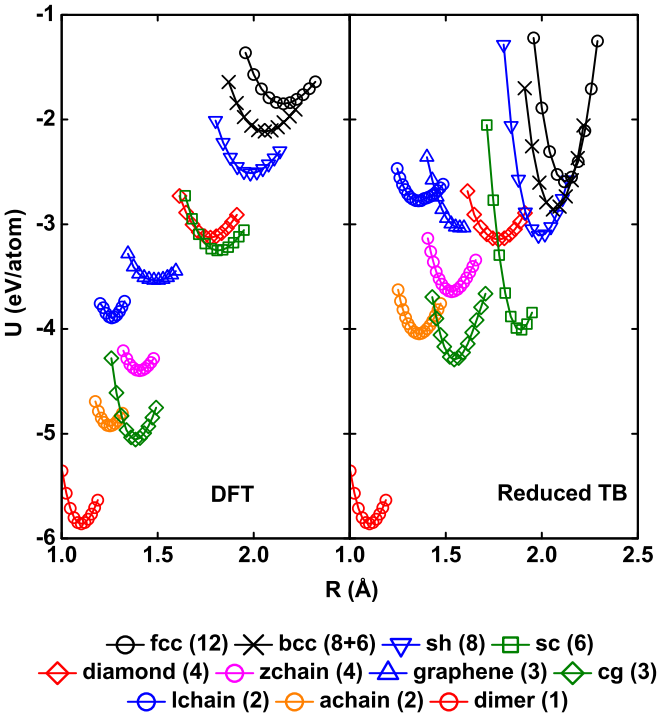

FIG. 11. (Color online) DFT and reduced TB (LCN) binding energy curves for different nitrogen structures as a function of nearest neighbor interatomic distance R. The number of nearest neighbors is given in parentheses for each structure.

structure, although both σ and π bonds in the sc structure are less saturated. Similar to the bond-order value of different silicon structures in Fig. 5, the bond-order value of different nitrogen structures varies inversely with the coordination number.

B. Binding energy curves

To be able to calculate binding energies for the nitrogen reduced TB model, a repulsive function is obtained as discussed previously for silicon. Figure 11 shows the reduced TB (LCN) binding energy curves for different nitrogen structures in the right-hand panel. As a comparison, the DFT binding energy curves are given in the left-hand panel. The parameters of the repulsive function for the nitrogen model are given in Table III. The embedding exponent, and the shift in the nonmagnetic DFT free atom reference energy are given in Table IV. For the nitrogen reduced TB (LCN) model no Yukawa-type core repulsion is used.

1. *DFT binding energy curves*

As expected, the DFT binding energy curves for nitrogen show that the dimer structure has the lowest binding energy. The lowest metastable structure is the threefold coordinated cubic gauche (cg) structure. This structure is a body centered cubic structure with four atoms per primitive cell. The second lowest metastable structure is the armchair chain (achain) structure with bond angles chosen to be 135 deg. The third lowest metastable structure is the zigzag chain (zchain) structure with bond angles of 90 deg. Even though this structure is a chainlike structure, it is fourfold coordinated due to the arrangement of the atoms resulting from the 90 deg bond angles. The fourth most stable metastable structure is the linear chain (lchain) structure. In this structure every atom has two nearest neighbors and it is equivalent to the zchain structure, but with bond angles of 180 deg. Overall, the DFT binding energy curves in Fig. 11 agree very well with Figs. 1 and 3 of Mailhiot *et al.* [86].

TABLE VIII. Equilibrium properties of the nitrogen dimer structure for reduced TB (LCN), DFT, and experiment. Equilibrium binding energy (U), equilibrium nearest neighbor distance (NND), and frequency ν are obtained from Birch-Murnaghan equation of state fits to binding energies. Units are U (eV/atom), NND (Å), ν (cm^{-1}). The pair of numbers in parentheses in the DFT column from Ref. [81] are LDA and GGA values, respectively.

	Reduced TB	DFT	Expt.	DFT [81]
U	−5.872	−5.860	−4.903[a]	(−5.666, −5.279)
NND	1.099	1.103	1.10[a], 1.112[b], 1.098[c]	(1.107, 1.113)
ν	2610	2615	2359[c], 2360[d], 2361[e]	(2465, 2351)

[a]Reference [82].
[b]Reference [83].
[c]Reference [84].
[d]Reference [85].
[e]Reference [81].

2. *Reduced TB binding energy curves*

As one can see from Fig. 11, the dimer structure is predicted to be the ground state structure by the reduced TB model. Moreover, the ordering dimer → cg → achain → zchain predicted by the DFT binding energy data is reproduced by the reduced TB model. In addition, the crossing of the diamond and the sc structures is reproduced. Furthermore, the ordering of the close packed structures sh → bcc → fcc is also reproduced by the reduced TB model. A table of nitrogen structures used as a binding energy benchmark with their binding energies is attached as Supplemental Material [75].

3. *Equilibrium properties of dimer ground state*

Table VIII gives equilibrium properties of the nitrogen dimer structure for reduced TB (LCN) and DFT calculated in this study. Experimental and DFT results from other studies are also included for comparison. Overall, the equilibrium properties of the dimer ground state predicted by the reduced TB model agree very well with the DFT calculations and results from other studies.

V. REDUCED TB MODEL FOR SILICON NITRIDE

In Secs. III and IV we introduced the elemental reduced TB (LCN) models for silicon and nitrogen within the constraint of local charge neutrality (LCN). We will use these elemental bond integrals and repulsive functions in the binary silicon nitride model without further adjustments. However, for the parametrization of the binary silicon nitride system, charge transfer (CT) is introduced as described in Sec. II A, so that all the silicon nitride figures correspond to the model allowing CT.

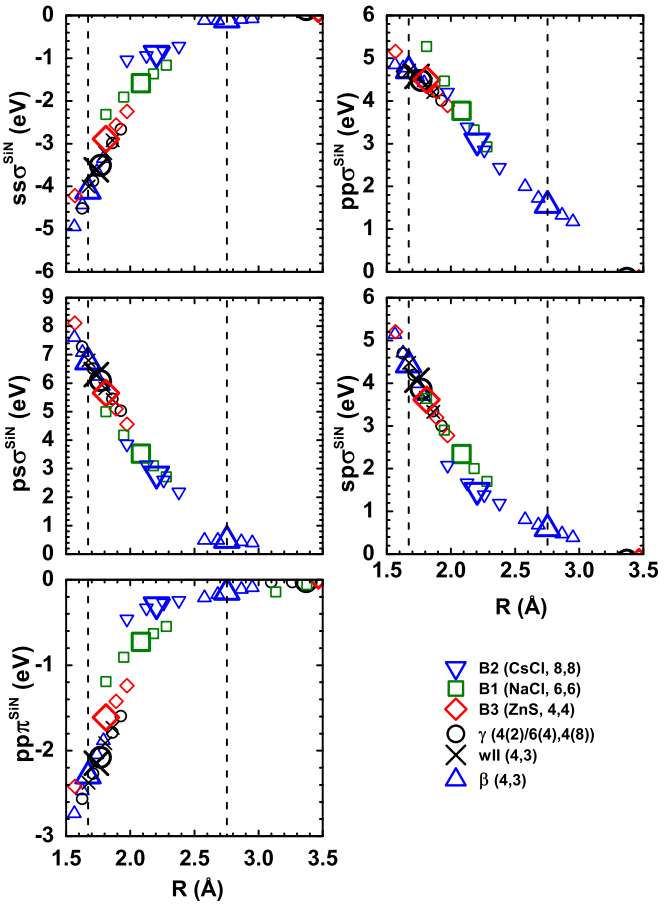

FIG. 12. (Color online) Two-center orthogonal TB Si-N bond integrals obtained from DFT via projection scheme for different structures as a function of interatomic distance R. Equilibrium data are displayed with enlarged symbols. Dashed vertical lines are the first and second nearest neighbor distances in the ground state equilibrium β structure, R_1^β and R_2^β. Note that the $ps\sigma$ data are multiplied by -1 to improve the comparability to the $sp\sigma$ data.

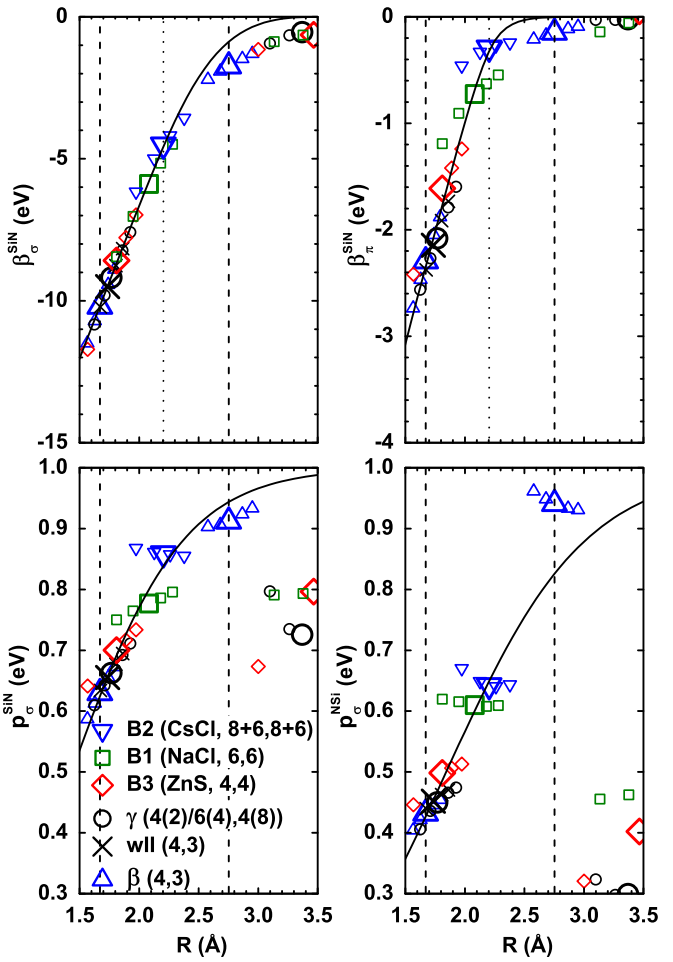

FIG. 13. (Color online) Reduced TB Si-N parameters calculated from projected bond integrals in Fig. 12 for different structures as a function of interatomic distance R. Equilibrium data are displayed with enlarged symbols. Dashed vertical lines are the first and second nearest neighbor distances in the ground state equilibrium β structure, R_1^β and R_2^β. The vertical dotted line marks R_{tail}.

A. Bond integrals

The two-center orthogonal TB Si-N bond integrals obtained from DFT for different structures are shown in Fig. 12. The data for equilibrium structures are displayed with enlarged symbols. Compared to the values for silicon and nitrogen, the values for silicon nitride are moderately structure dependent. Screening of second nearest neighbors can be observed in all the data.

Figure 13 displays the reduced TB parameters calculated from the data in Fig. 12. The first nearest neighbor values for p_σ^{NSi} are smaller than those for p_σ^{SiN}. This difference is obvious when considering the definition of p_σ^{SiN} and p_σ^{NSi} according to Eq. (46) and the different behavior of $ss\sigma^{\text{SiN}}$, $pp\sigma^{\text{SiN}}$, $sp\sigma^{\text{SiN}}$, $ps\sigma^{\text{SiN}}$, and $pp\pi^{\text{SiN}}$ in Fig. 12.

The functions $\beta_\sigma(R)$, $\beta_\pi(R)$, and $p_\sigma(R)$ in Fig. 13 are fitted to equilibrium data points, with the same considerations as for the elemental models. The functions $\beta_\sigma(R)$ and $\beta_\pi(R)$ reproduce the data as well as the gradients of the individual structures fairly well. For the same reason as given for the elemental models, $p_\sigma^{\text{SiN}}(R)$ and $p_\sigma^{\text{NSi}}(R)$ are chosen to be constants.

The parameters of the functions representing the reduced TB parameters for the silicon nitride TB model are given in Table I. The species dependent atomic on-site Coulomb integrals for silicon and nitrogen required for the inclusion of charge transfer are given in Table IX.

Figure 14 shows the average total density of states of the silicon nitride β structure for DFT, projected TB, and reduced TB. The local s and p contributions of silicon and nitrogen to the average total density of states are also displayed. The features of the DFT density of states are qualitatively reproduced by projected TB and reduced TB.

The nearest neighbor σ and π bond orders of silicon nitride in the β structure are given by $\Theta_\sigma = 0.84$, $\Theta_{\pi+} = 0.27$, and

TABLE IX. Species dependent atomic on-site Coulomb integrals for silicon (Si) and nitrogen (N) [55].

	Si	N
J (eV/e^2)	7.095	11.919

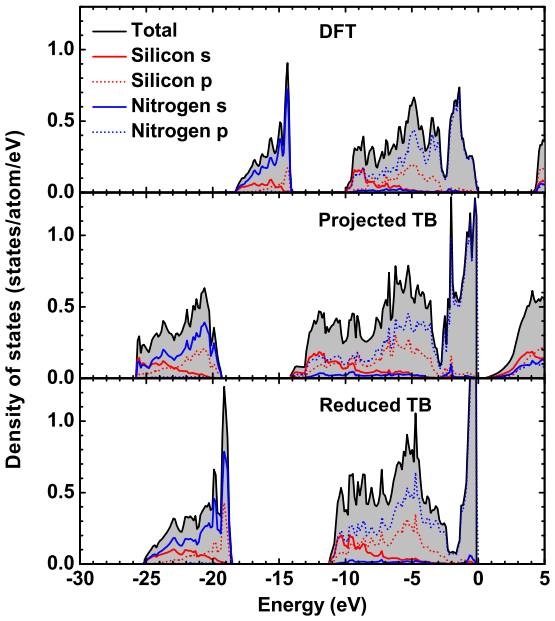

FIG. 14. (Color online) Local *s* and *p* contributions of silicon and nitrogen to the average total density of states of the silicon nitride β structure for DFT, projected TB, and reduced TB. For the calculation of the projected TB DOS the same on-site levels were used as for the calculation of the reduced TB DOS.

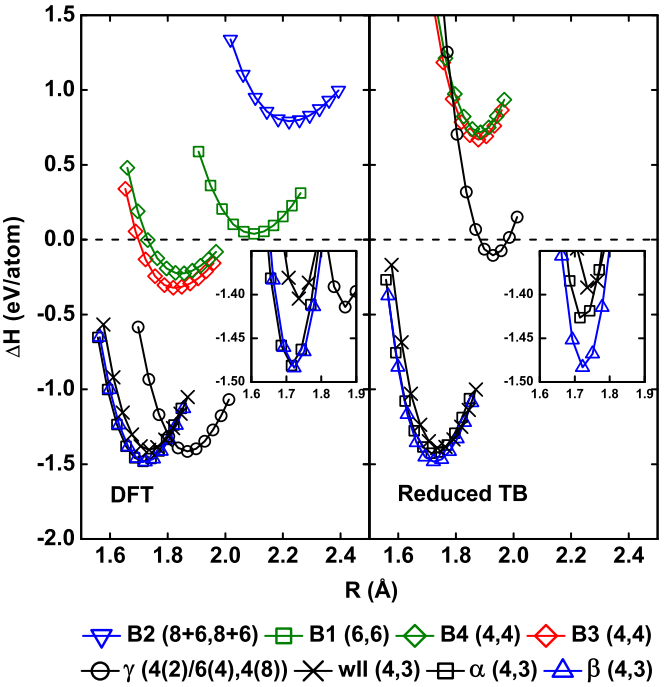

FIG. 15. (Color online) DFT and reduced TB (CT) heat of formation curves for different silicon nitride structures as a function of nearest neighbor interatomic distance *R*. The number of nearest neighbors is given in parentheses for each structure.

$\Theta_{\pi-} = 0.18$. In the β structure each silicon atom is surrounded by four neighboring nitrogen atoms and each nitrogen atom is surrounded by three neighboring silicon atoms. Therefore, each silicon atom provides one valence electron to each of the four silicon-nitrogen bonds around silicon and each nitrogen atom contributes five valence electrons to the three silicon-nitrogen bonds around nitrogen.

The specific values for the difference in the charge compared to the respective free atoms in the β equilibrium structure are in our study -1.314 electrons per atom for silicon, and $+0.990$ and $+0.973$ electrons per atom for the two nitrogen sites N1 and N2, respectively. These values agree very well with the values from the study by Zhao *et al.* [87] who investigated the electronic structure and charge transfer at the silicon-silicon nitride interface using LDA and calculated an average of -1.24 electrons per silicon atom and $+0.93$ electrons per nitrogen atom for the α and β structures.

B. Heat of formation curves

Figure 15 shows the reduced TB (CT) heat of formation curves for different silicon nitride structures in the right-hand panel. As a comparison, the DFT heat of formation curves are displayed in the left-hand panel of Fig. 15. The parameters of the repulsive function for the silicon nitride reduced TB (CT) model are given in Table III. The elemental embedding exponents, the elemental shifts in the nonmagnetic DFT free atom reference energy, and the binary Yukawa parameters are given in Tables IV and V.

1. DFT heat of formation curves

The DFT heat of formation curves in Fig. 15 show the Si_3N_4 β phase as the ground state structure. The second lowest structure is α with a 0.0025 eV/atom higher equilibrium heat of formation value. This value is consistent with the marginal difference in experimental heat of formation values between these two polytypes [88], and is responsible for the ability to experimentally achieve these two hexagonal crystal structures, which differ only by their stacking sequence, with different processing routes [89]. For both structures the basic building block is a silicon-nitrogen tetrahedron with a silicon atom at its center and four nitrogen atoms at each vertex. All these SiN_4 tetrahedra are linked by nitrogen atoms which are each common to three tetrahedra. As a result each silicon atom has four nitrogen atoms as nearest neighbors and each nitrogen atom has three silicon atoms as nearest neighbors. Therefore, the notation β (4,3) was chosen, where 4 is the number of nearest neighbors of each silicon atom and 3 is the number of nearest neighbors of each nitrogen atom. The third lowest structure predicted by DFT is the cubic γ structure [90] and the fourth lowest structure is the willemite-II (wII) structure [91]. Both structures have the same chemical composition as the β and α structures. In the γ structure, two of the six silicon atoms have four nearest neighbors, and the other four silicon atoms have six nearest neighbors. All eight nitrogen atoms have four nearest neighbors. Therefore, we chose the notation γ (4(2)/6(4),4(8)). The SiN phases B1, B2, B3, and B4 are the structures NaCl, CsCl, ZnS, and wurtzite, respectively. From the DFT heat of formation curves the ordering $\beta \rightarrow \alpha \rightarrow \gamma \rightarrow$ wII $\rightarrow$ B3 $\rightarrow$ B4 $\rightarrow$ B1 $\rightarrow$ B2 can be observed.

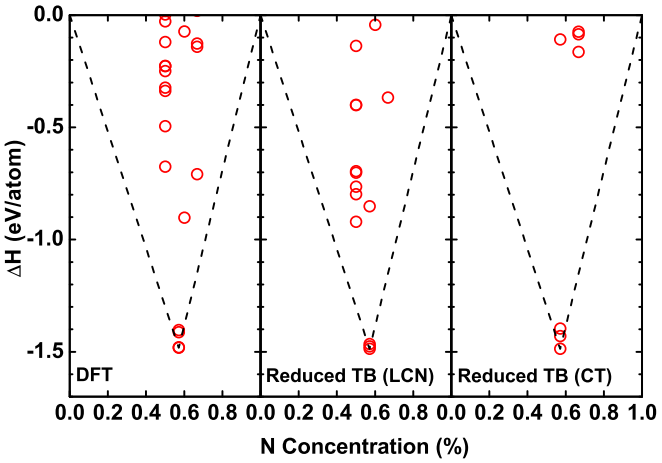

FIG. 16. (Color online) Heat of formation for different silicon nitride structures for DFT, reduced TB (LCN), and reduced TB (CT), versus nitrogen concentration.

2. *Reduced TB heat of formation curves*

As one can see from Fig. 15, the β structure is predicted to be the ground state structure by the reduced TB (CT) model. Furthermore, the ordering of the different SiN phases is in good agreement with the DFT results. Especially, the ordering over similar nearest neighbor distances and composition of $\beta \rightarrow \alpha \rightarrow$ wII predicted by the DFT heat of formation data is reproduced by the reduced TB model. In addition, the ordering of the high heat of formation structures, namely B3 $\rightarrow$ B4 $\rightarrow$ B1 $\rightarrow$ B2 is being reproduced. The reduced TB model predicts heat of formation values for B1 and B2 that are out of the scale of the right-hand panel of Fig. 15. See Table III in the Supplemental Material [75] for a comparison of the heat of formation values of the silicon nitride structures used as a benchmark.

The heat of formation values of these silicon nitride benchmark structures for DFT, reduced TB (LCN), and reduced TB (CT), versus nitrogen concentration are shown in Fig. 16. All three methods reproduce the fact that Si_3N_4 is the only well-established stoichiometric compound found experimentally in the silicon nitride binary system [92].

Figure 17 shows the binding energy contributions according to Eq. (22) for different silicon nitride structures for the reduced TB (CT) model. By considering the individual contributions to the binding energy for the structures β, α, and wII, the driving factors for the relative stability can be examined. For example, the ordering $\beta \rightarrow \alpha$ can be mainly attributed to the bond energy. At β equilibrium nearest neighbor distance, the bond energy contributes to the stabilization of the β structure compared to the α structure with 0.420 eV/atom. Furthermore, a marginal stabilization of the β structure compared to the α structure can be observed in the $U_{\text{ion}}^{\text{intra}}$ and $U_{\text{ion}}^{\text{inter}}$ energy contributions, which both have a stabilization effect of 0.004 eV/atom. The fact that the reduced TB model is able to destabilize the wII structure compared to the β and α structures can be mainly attributed to the repulsive energy, with 0.318 eV/atom being the difference in repulsive

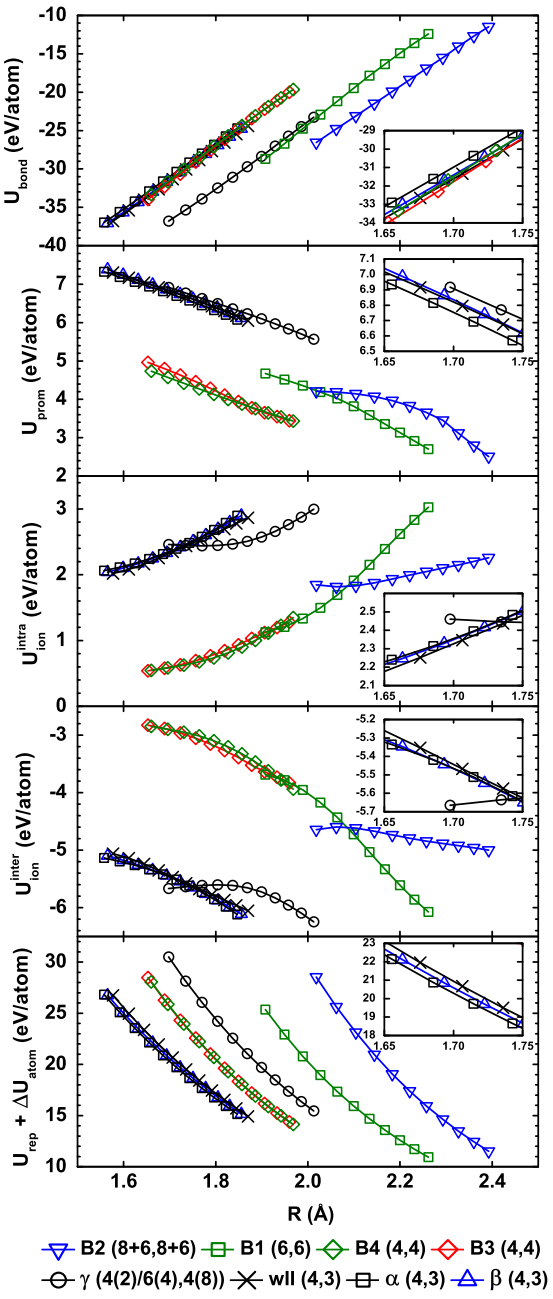

FIG. 17. (Color online) Binding energy contributions for different silicon nitride structures for reduced TB (CT) as a function of interatomic distance R.

energy between the wII and the β structure. In addition, $U_{\text{ion}}^{\text{inter}}$ has a tiny effect with 0.022 eV/atom, too. Even though our model reproduces the fact that charge transfer is present in silicon nitride, the contributions $U_{\text{ion}}^{\text{intra}}$ and $U_{\text{ion}}^{\text{inter}}$ to the binding energy seem to have only a minor effect on the relative ordering $\beta \rightarrow \alpha \rightarrow$ wII.

3. *Equilibrium properties of β phase ground state*

Table X gives equilibrium properties of the silicon nitride β structure for reduced TB (CT) and DFT. The reduced TB heat of formation, equilibrium volume, and bulk modulus are

TABLE X. Equilibrium properties of the silicon nitride β structure for reduced TB (CT) and DFT. Equilibrium heat of formation (ΔH), equilibrium volume (V), and bulk modulus (B) are obtained from Birch-Murnaghan equation of state fits to binding energies. Units are ΔH (eV/atom), V (Å^3), B and C (GPa). The FF column displays values of the force field at 0 K and B is calculated from other elastic constants.

	Reduced TB	DFT	Expt.	DFT	FF [93]
ΔH	−1.487	−1.483	−1.261[a]	b	b
V	10.331	10.290	(10.423, 10.410, 10.423, 10.400)[c]	(10.647, 10.303)[d], 10.302[e], 10.619[f]	9.978, 10.429, 10.454
B	303	254	273[g]	270[e], 234[f]	285
$C11$	410	423	343[h]	409[e], 413[f]	448
$C12$	191[i]	200[i]	136[h]	271[e], 198[f]	215
$C13$	91[i]	117[i]	120[h]	201[e], 116[f]	165
$C33$	591	553	600[h]	604[e], 544[f]	580
$C44$	93	99	124[h]	108[e], 99[f]	115

[a]Reference [88].
[b]Not available.
[c]Reference [94].
[d]Reference [95] (GGA, LDA).
[e]Reference [96] method: Orthogonalized linear combination of atomic orbitals (OLCAO) approach based on DFT/LDA.
[f]Reference [41] (GGA).
[g]Reference [97].
[h]Reference [98].
[i]Calculated from results of C11 − C12 and C11 + C33 − 2C13 deformations.

in good agreement with the DFT results. In addition, the elastic constants are fairly well reproduced. Experimental data, DFT results from other studies, and results from force field calculations are also included for comparison.

To our knowledge, studies of simple point defects in pure crystalline silicon nitride have not been discussed in the literature, which may be due to the fact that defects like elemental bond formation are not found experimentally in stoichiometric silicon nitride [99]. More frequently found defects include oxygen [94] and hydrogen [99] contaminations. Therefore, we test our silicon nitride reduced TB (CT) model for point defects only to compare with DFT results and not to reproduce experimental values.

Table XI gives relaxed point defect formation energies in silicon nitride β (eV) with 112 atoms per perfect unit cell. N1 and N2 correspond to the two different nitrogen atomic sites in the β structure. Overall, the formation energies calculated with the reduced TB model are comparable to the values obtained with DFT.

TABLE XI. Relaxed point defect formation energies in silicon nitride β (eV) with 112 atoms per perfect unit cell.

	Reduced TB (112)	DFT (112)
Si vacancy	9.612	10.843
N1 vacancy	6.205	5.692
N2 vacancy	5.991	6.126
Si(N1) antisite	13.892	11.972
Si(N2) antisite	12.000	10.823

VI. CONCLUSIONS

We show that by coarse graining the electronic structure from density functional theory (DFT) to tight binding (TB) and with the help of the reduced TB approximation a transferable model for the silicon nitride system can be developed. Within this approach the TB bond integrals are obtained directly from DFT projections which thereby reduces the number of overall parameters to be fitted. Furthermore, we show that the reduced TB approximation is not only the theoretical link between the quantum mechanical DFT and the bond-based BOPs, but, in addition, provides a decent description of the silicon nitride system. The binding energies, heats of formation, elastic constants, and defect energies calculated with our reduced TB models are in reasonable agreement with DFT calculations and experimental values. In addition, applying bond-order potential (BOP) theory, an analytic interatomic potential may be derived directly from this reduced TB description of the electronic structure. The parameters from the reduced TB model are suitable as input for the individual BOP energy contributions. Preliminary results for silicon are given in the first author's Ph.D. thesis [59].

ACKNOWLEDGMENTS

We would like to thank our collaborators in the nanocoatings project, especially Paul Kamenski, Elena Roxana Margine, Bernd Meyer, Alexander Urban, Joerg Patscheider, and Dominik Jaeger. Furthermore, we would like to thank Thomas Hammerschmidt for his help with code development. J.G. thanks the Engineering and Physical Sciences Research Council (EPSRC) of the United Kingdom for funding. M.R., M.M., and C.E. acknowledge financial support from the German Research Foundation (DFG) via Grant No. MR 22/5-1,2.

[1] H. Hauser, Thermochim. Acta **112**, 1 (1987).
[2] C. Juang, J. H. Chang, and R. Y. Hwang, J. Vac. Sci. Technol. B **10**, 1221 (1992).
[3] E. Kroke and M. Schwarz, Coord. Chem. Rev. **248**, 493 (2004).
[4] A. Kailer, Konstruk. Z. Prod. Ingenieur-Werkstoffe **7–8**, IW8 (2010).
[5] F. L. Riley, J. Am. Ceram. Soc. **83**, 245 (2000).
[6] S. Hampshire, J. Achieve. Mater. Manuf. Eng. **24**, 43 (2007).
[7] R. C. Buchanan, eds., *Ceramic Materials for Electronics*, 3rd ed. (Marcel Dekker, New York, 2004).
[8] R.-H. Ma, P.-C. Chou, Y.-H. Wang, T.-H. Hsueh, L.-M. Fu, and C.-Y. Lee, Microsyst. Technol. **15**, 1201 (2009).
[9] W. van Gelder and V. E. Hauser, J. Electrochem. Soc. **114**, 869 (1967).
[10] A. Piccirillo and A. L. Gobbi, J. Electrochem. Soc. **137**, 3910 (1990).
[11] H. O. Pierson, *Handbook of Chemical Vapor Deposition (CVD): Principles, Technology, and Applications* (William Andrew, Norwich, New York, 1992).
[12] C. Uslu, B. Park, and D. B. Poker, J. Electron. Mater. **25**, 23 (1996).
[13] M. Lattemann, S. Ulrich, H. Holleck, M. Stüber, and H. Leiste, Diamond Relat. Mater. **11**, 1248 (2002).
[14] D. Pakuła, L. A. Dobrzański, K. Gołombek, M. Pancielejko, and A. Kříž, J. Mater. Process. Tech. **157–158**, 388 (2004).
[15] J. Robertson, Philos. Mag. B **44**, 215 (1981).
[16] J. Robertson and M. J. Powell, Appl. Phys. Lett. **44**, 415 (1984).
[17] J. Robertson, Philos. Mag. B **63**, 47 (1991).
[18] J. Robertson, Philos. Mag. B **69**, 307 (1994).
[19] J. Robertson, W. L. Warren, and J. Kanicki, J. Non-Cryst. Solids **187**, 297 (1995).
[20] J. Tersoff, Phys. Rev. Lett. **56**, 632 (1986).
[21] P. Vashishta, R. K. Kalia, J. P. Rino, and I. Ebbsjö, Phys. Rev. B **41**, 12197 (1990).
[22] F. de Brito Mota, J. F. Justo, and A. Fazzio, Phys. Rev. B **58**, 8323 (1998).
[23] F. De Brito Mota, J. F. Justo, and A. Fazzio, Int. J. Quantum Chem. **70**, 973 (1998).
[24] F. de Brito Mota, J. F. Justo, and A. Fazzio, J. Appl. Phys. **86**, 1843 (1999).
[25] F. Gou, M. Gleeson, A. Kleyn, R. van de Kruijs, A. Yakshin, and F. Bijkerk, Nucl. Instrum. Methods B **267**, 3245 (2009).
[26] J. Houska, J. E. Klemberg-Sapieha, and L. Martinu, J. Appl. Phys. **107**, 083501 (2010).
[27] A.-P. Prskalo, S. Schmauder, C. Ziebert, J. Ye, and S. Ulrich, Surf. Coat. Technol. **204**, 2081 (2010).
[28] F. H. Stillinger and T. A. Weber, Phys. Rev. B **31**, 5262 (1985).
[29] A. Nakano, R. K. Kalia, and P. Vashishta, Phys. Rev. Lett. **75**, 3138 (1995).
[30] P. Vashishta, R. K. Kalia, A. N. Weili, and I. Ebbsjö, NATO ASI Ser. 3 Technol. **23**, 151 (1996).
[31] R. K. Kalia, A. Nakano, A. Omeltchenko, K. Tsuruta, and P. Vashishta, Phys. Rev. Lett. **78**, 2144 (1997).
[32] P. Vashishta, A. Nakano, R. K. Kalia, and I. Ebbsjö, J. Non-Cryst. Solids **182**, 59 (1995).
[33] R. K. Kalia, A. Nakano, K. Tsuruta, and P. Vashishta, Phys. Rev. Lett. **78**, 689 (1997).
[34] S. Ogata, H. Kitagawa, N. Hirosaki, Y. Hatanaka, and T. Umezu, Comp. Mater. Sci. **23**, 146 (2002).
[35] M. E. Bachlechner, A. Omeltchenko, A. Nakano, R. K. Kalia, P. Vashishta, I. Ebbsjö, A. Madhukar, and P. Messina, Appl. Phys. Lett. **72**, 1969 (1998).
[36] X.-Y. Guo and P. Brault, Surf. Sci. **488**, 133 (2001).
[37] R. Belkada, T. Shibayanagi, M. Naka, and M. Kohyama, J. Am. Ceram. Soc. **83**, 2449 (2000).
[38] W. Y. Ching, L. Ouyang, and J. D. Gale, Phys. Rev. B **61**, 8696 (2000).
[39] R. Belkada, M. Kohyama, T. Shibayanagi, and M. Naka, Phys. Rev. B **65**, 092104 (2002).
[40] A. Togo and P. Kroll, J. Comput. Chem. **29**, 2255 (2008).
[41] T. Watts, Diplomarbeit, Universität Wien, 2011.
[42] R. Drautz, X. W. Zhou, D. A. Murdick, B. Gillespie, H. N. G. Wadley, and D. G. Pettifor, Prog. Mater. Sci. **52**, 196 (2007).
[43] R. Drautz and D. G. Pettifor, Phys. Rev. B **84**, 214114 (2011).
[44] D. A. Murdick, X. W. Zhou, H. N. G. Wadley, D. Nguyen-Manh, R. Drautz, and D. G. Pettifor, Phys. Rev. B **73**, 045206 (2006).
[45] B. A. Gillespie, X. W. Zhou, D. A. Murdick, H. N. G. Wadley, R. Drautz, and D. G. Pettifor, Phys. Rev. B **75**, 155207 (2007).
[46] A. Urban, M. Reese, M. Mrovec, C. Elsässer, and B. Meyer, Phys. Rev. B **84**, 155119 (2011).
[47] G. K. H. Madsen, E. J. McEniry, and R. Drautz, Phys. Rev. B **83**, 184119 (2011).
[48] D. G. Pettifor, *Bonding and Structure of Molecules and Solids* (Oxford Science, New York, 2002).
[49] M. Elstner, D. Porezag, G. Jungnickel, J. Elsner, M. Haugk, T. Frauenheim, S. Suhai, and G. Seifert, Phys. Rev. B **58**, 7260 (1998).
[50] O. K. Andersen and O. Jepsen, Phys. Rev. Lett. **53**, 2571 (1984).
[51] J. C. Slater and G. F. Koster, Phys. Rev. **94**, 1498 (1954).
[52] E. R. Margine, A. N. Kolmogorov, M. Reese, M. Mrovec, C. Elsässer, B. Meyer, R. Drautz, and D. G. Pettifor, Phys. Rev. B **84**, 155120 (2011).
[53] L. Goodwin, A. J. Skinner, and D. G. Pettifor, Europhys. Lett. **9**, 701 (1989).
[54] M. Aoki, D. Nguyen-Manh, D. G. Pettifor, and V. Vitek, Prog. Mater. Sci. **52**, 154 (2007).
[55] C. Köhler, Ph.D. thesis, Department Physik der Fakultät für Naturwissenschaften an der Universität Paderborn, 2003.
[56] T. S. Hudson, D. Nguyen-Manh, A. C. T. van Duin, and A. P. Sutton, Mater. Sci. Eng. A **422**, 123 (2006).
[57] D. G. Pettifor, Springer Proc. Phys. **48**, 64 (1990).
[58] D. G. Pettifor, M. W. Finnis, D. Nguyen-Manh, D. A. Murdick, X. W. Zhou, and H. N. G. Wadley, Mater. Sci. Eng. A **365**, 2 (2004).
[59] J. Gehrmann, Ph.D. thesis, University of Oxford, Oxford, 2013.
[60] G. Kresse and J. Hafner, Phys. Rev. B **47**, 558 (1993).
[61] G. Kresse and J. Furthmuller, Phys. Rev. B **54**, 11169 (1996).
[62] D. M. Ceperley and B. J. Alder, Phys. Rev. Lett. **45**, 566 (1980).
[63] J. P. Perdew and A. Zunger, Phys. Rev. B **23**, 5048 (1981).
[64] P. E. Blöchl, Phys. Rev. B **50**, 17953 (1994).
[65] G. Kresse and D. Joubert, Phys. Rev. B **59**, 1758 (1999).
[66] H. J. Monkhorst and J. D. Pack, Phys. Rev. B **13**, 5188 (1976).
[67] J. D. Pack and H. J. Monkhorst, Phys. Rev. B **16**, 1748 (1977).
[68] T. Hammerschmidt, B. Seiser, M. E. Ford, D. G. Pettifor, and R. Drautz (unpublished).
[69] P. E. Blöchl, O. Jepsen, and O. K. Andersen, Phys. Rev. B **49**, 16223 (1994).

[70] D. Nguyen-Manh, D. G. Pettifor, and V. Vitek, Phys. Rev. Lett. **85**, 4136 (2000).
[71] C. H. Xu, C. Z. Wang, C. T. Chan, and K. M. Ho, J. Phys.: Condens. Matter **4**, 6047 (1992).
[72] I. Kwon, R. Biswas, C. Z. Wang, K. M. Ho, and C. M. Soukoulis, Phys. Rev. B **49**, 7242 (1994).
[73] W. A. Harrison, *Elementary Electronic Structure (Revised Edition)* (World Scientific, Singapore, 2004).
[74] R. Drautz, D. A. Murdick, D. Nguyen-Manh, X. Zhou, H. N. G. Wadley, and D. G. Pettifor, Phys. Rev. B **72**, 144105 (2005).
[75] See Supplemental Material at http://link.aps.org/supplemental/10.1103/PhysRevB.91.054109 for silicon, nitrogen, and silicon nitride structures used as binding energy and heat of formation benchmark.
[76] T. J. Lenosky, J. D. Kress, I. Kwon, A. F. Voter, B. Edwards, D. F. Richards, S. Yang, and J. B. Adams, Phys. Rev. B **55**, 1528 (1997).
[77] H. Balamane, T. Halicioglu, and W. A. Tiller, Phys. Rev. B **46**, 2250 (1992).
[78] http://www.webelements.com/silicon/physics.html
[79] G. Simmons and H. Wang, *Single Crystal Elastic Constants and Calculated Aggregate Properties: A Handbook*, 2nd ed. (MIT Press, Cambridge, MA, 1971).
[80] R. J. Needs, J. Phys.: Condens. Matter **11**, 10437 (1999).
[81] A. Zoroddu, F. Bernardini, P. Ruggerone, and V. Fiorentini, Phys. Rev. B **64**, 045208 (2001).
[82] http://www.zum.de/faecher/materialien/beck/chemkurs/cs11-14.htm
[83] http://www.colby.edu/chemistry/webmo/n2.html
[84] K. Huber, *Constants of Polyatomic Molecules* (Van Nostrand Reinhold, Amsterdam, 1979).
[85] C. Stampfl and C. G. Van de Walle, Phys. Rev. B **59**, 5521 (1999).
[86] C. Mailhiot, L. H. Yang, and A. K. McMahan, Phys. Rev. B **46**, 14419 (1992).
[87] G. L. Zhao and M. E. Bachlechner, Phys. Rev. B **58**, 1887 (1998).
[88] J. Liang, L. Topor, A. Navrotsky, and M. Mitomo, J. Mater. Res. **14**, 1959 (1999).
[89] E. T. Turkdogan, P. M. Bills, and V. A. Tippett, J. Appl. Chem. **8**, 296 (1958).
[90] A. Zerr, G. Miehe, G. Serghiou, M. Schwarz, E. Kroke, R. Riedel, H. Fue, P. Kroll, and R. Boehler, Nature (London) **400**, 340 (1999).
[91] P. Kroll, J. Solid State Chem. **176**, 530 (2003).
[92] X. Ma, C. Li, F. Wang, and W. Zhang, CALPHAD Comput. Coupling Phase Diagrams Thermochem. **27**, 383 (2003).
[93] J. A. Wendel and W. A. Goddard, J. Chem. Phys. **97**, 5048 (1992).
[94] C.-M. Wang, X. Pan, M. Rühle, F. L. Riley, and M. Mitomo, J. Mater. Sci. **31**, 5281 (1996).
[95] J. C. Idrobo, H. Iddir, S. Ogut, A. Ziegler, N. D. Browning, and R. O. Ritchie, Phys. Rev. B **72**, 241301 (2005).
[96] W.-Y. Ching, Y.-N. Xu, J. D. Gale, and M. Rühle, J. Am. Ceram. Soc. **81**, 3189 (1998).
[97] Y. M. Li, M. B. Kruger, J. H. Nguyen, W. A. Caldwell, and R. Jeanloz, Solid State Commun. **103**, 107 (1997).
[98] J. C. Hay, E. Y. Sun, G. M. Pharr, P. F. Becher, and K. B. Alexander, J. Am. Ceram. Soc. **81**, 2661 (1998).
[99] L. E. Hintzsche, C. M. Fang, T. Watts, M. Marsman, G. Jordan, M. W. P. E. Lamers, A. W. Weeber, and G. Kresse, Phys. Rev. B **86**, 235204 (2012).